HHS Public Access

Author manuscript

Mol Cell. Author manuscript; available in PMC 2024 October 19.

Published in final edited form as:

Mol Cell. 2023 October 19; 83(20): 3692–3706.e5. doi:10.1016/j.molcel.2023.09.024.

Sen1 Architecture: RNA-DNA Hybrid Resolution, Autoregulation, and Insights into SETX Inactivation in AOA2

C. Denise Appel[1,3], **Oya Bermek**[1,3], **Venkata P. Dandey**[1], **Makayla Wood**[1], **Elizabeth Viverette**[1], **Jason G. Williams**[2], **Jonathan Bouvette**[1], **Amanda A. Riccio**[1], **Juno M. Krahn**[1], **Mario J. Borgnia**[1], **R. Scott Williams**[1,4,*]

[1]Genome Integrity and Structural Biology Laboratory, National Institute of Environmental Health Sciences, National Institutes of Health, Department of Health and Human Services, Research Triangle Park, NC, 27709, USA

[2]Epigenetics and Stem Cell Laboratory, National Institute of Environmental Health Sciences, National Institutes of Health, Department of Health and Human Services, Research Triangle Park, NC, 27709, USA

[3]These authors contributed equally.

[4]Lead contact

SUMMARY

The Senataxin (SETX, Sen1 in yeasts) RNA-DNA hybrid resolving helicase regulates multiple nuclear transactions including DNA replication, transcription, and DNA repair, but the molecular basis for Sen1 activities is ill-defined. Here, Sen1 cryo-EM reconstructions reveal an elongated inchworm-like architecture. Sen1 is comprised of an amino terminal helical repeat Sen1 N-terminal (Sen1N) regulatory domain that is flexibly linked to its C-terminal SF1B helicase motor core ($Sen1^{Hel}$) via an intrinsically disordered tether. In an autoinhibited state, the $Sen1^{Sen1N}$ domain regulates substrate engagement by promoting occlusion of the RNA substrate binding cleft. The X-ray structure of an activated $Sen1^{Hel}$ engaging single-stranded RNA and ADP-SO_4 shows the enzyme encircles RNA and implicates a single nucleotide power stroke in the Sen1 RNA translocation mechanism. Together, our data unveil dynamic protein-protein and protein-RNA interfaces underpinning helicase regulation and inactivation of human SETX activity by RNA-binding deficient mutants in Ataxia with Oculomotor Apraxia 2 neurodegenerative disease.

Graphical Abstract

*Correspondence: williamsrs@niehs.nih.gov.

AUTHOR CONTRIBUTIONS

Conceptualization, R.S.W., C.D.A.; Methodology, J.B., M.J.B., C.D.A., O.B, R.S.W; Investigation, C.D.A., O.B., A.A.R., E.V., M.W., R.S.W.; Formal Analysis, C.D.A., O.B. V.P.D., A.A.R., J.M.K., R.S.W.; Writing – Original Draft, C.D.A., O.B., R.S.W.; Writing – Review & Editing, C.D.A., O.B., A.A.R., R.S.W.; Resources and Supervision, R.S.W., V.P.D. and M.J.B.

DECLARATION OF INTERESTS

The authors declare no competing interests.

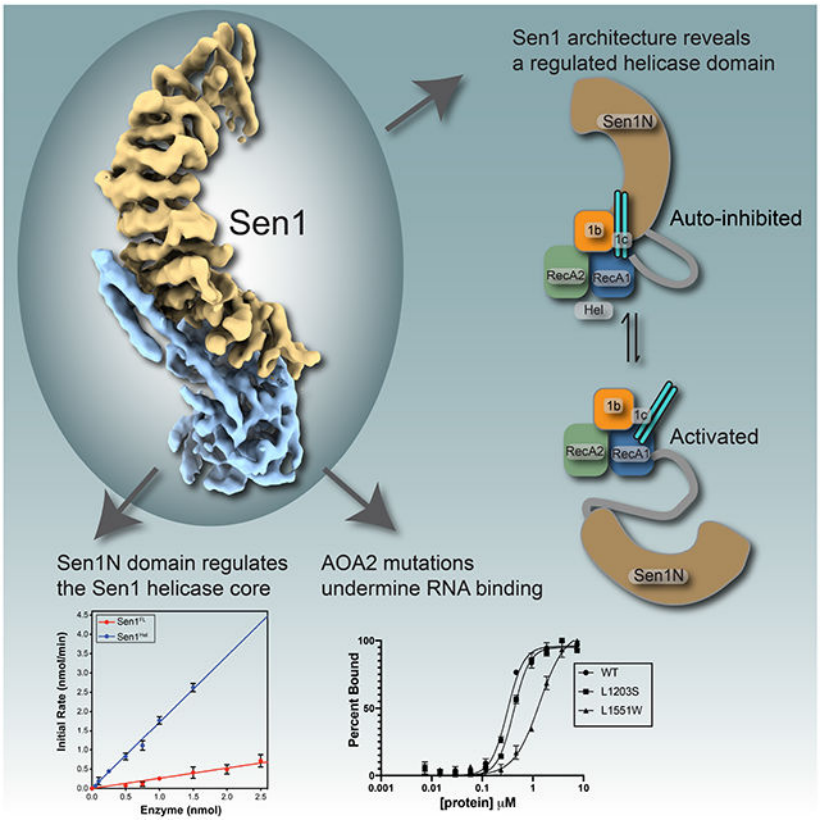

eTOC Blurb

Sen1/SETX helicases resolve RNA-DNA hybrids to regulate transcription, DNA replication and DNA repair. Appel *et al* solve cryo-EM and X-ray crystal structures of Sen1-RNA complexes showing how the enzyme is auto-regulated, and report how Sen1/SETX can be inactivated by AOA2 RNA binding cleft mutants.

Keywords

Sen1; SETX; Senataxin; cryo-EM; X-ray crystallography; RNA-DNA hybrid; R-loop; Helicase; SF1B; DNA repair; transcription

INTRODUCTION

R-loops form when a nascent transcribed RNA pairs with its DNA template to displace the non-template DNA strand that becomes extruded as single stranded DNA (ssDNA). R-loops can occur during normal transcription, when topoisomerase reactions are perturbed, during replication-transcription collisions, and also at DNA double strand breaks[1-3]. Multiple lines of evidence implicate the RNA-DNA hybrid resolving Senataxin (SETX, Sen1 in yeast) helicase in the regulation of R-loops[1-3]. Yeast Sen1 participates in RNA processing, DNA replication, transcription termination, and DNA repair[3-5]. DNA repair roles are consistent with human SETX deficient cells showing marked sensitivity to DNA damaging agents including mitomycin C, camptothecin, H_2O_2[6] and the anticancer Top2 poison etoposide[7].

Sen1/SETX orthologs also cooperate with the Mre11-Rad50-Nbs1 complex in double strand break (DSB) repair in yeast[8] and mammalian cells[9], and human SETX limits illegitimate DNA end-joining of DSB ends produced in actively transcribed genes [7]. A role for Sen1 activity in resolving RNA-DNA hybrids during S-phase is consistent with its functions in preventing genome instability arising from replication/transcription collisions[10]. Autosomal recessive mutations in human Senataxin (*SETX*) cause Ataxia-Oculomotor-Apraxia 2 (AOA2), whereas dominant *SETX* mutations are linked to Amyotrophic Lateral Sclerosis Type 4 (ALS4)[11,12] (Supplementary Table 1). How SETX mutations cause disease remains poorly defined.

The Sen1 polypeptide broadly segments by homology into N- and C-terminal halves. The N-terminal Sen1^{Sen1N} region is a protein-protein interaction domain[4]. Deletion of the Sen1N region of budding yeast Sen1 results in both heat and cold temperature sensitive growth phenotypes, whereas the catalytic core is essential. Both the N- and C-terminal Sen1 domains are requisite for robust transcription termination function[13]. Sen1 binds the RNA polymerase II large subunit (Rpb1) through its N-terminal region[4], regulates transcriptional termination, modulates genome-wide of RNA polymerase II distribution on protein-coding and non-coding genes[14]. Sen1 also directly binds Nrd1-Nab3[15] and this Nrd1–Nab3–Sen1 (NNS) complex functions in a poly(A)-independent mechanism of transcription termination of non-coding snoRNA, snRNAs and cryptic unstable transcripts[16-18]. In this context it is hypothesized Sen1 helicase activity promotes displacement of Pol II from the DNA template[14,18].

Consistent with its roles in promoting genome stability during replication, Sen1^{Sen1N} binds Ctf4[19], a DNA replisome protein-protein interaction hub[20,21]. *Sen1*^{Sen1N} mutants impair association with the replisome and confer a synthetic lethal phenotype in the context of deletion of RNase H1 (*RNH1*) and RNase H2 (*RNH201*) RNA-DNA hybrid metabolism genes and show increased genome instability and recombination. The C-terminal superfamily I (SF1) helicase domain (Sen1^{Hel})[22] has ATP-stimulated DNA and RNA dependent 5′-3′ DNA translocation and unwinding activities[23-25]. Sen1^{Sen1N} also regulates helicase and RNA-DNA stimulated ATPase activities[23,24]. The X-ray crystal structure of the ADP-bound catalytic core of *S. cerevisiae* Sen1 revealed the enzyme is structurally related to the eukaryotic nonsense mediated decay Upf1 protein[23]. However, despite the broadly implicated roles for Sen1 in DNA and RNA metabolism, the molecular basis for Sen1 *cis*- and *trans*- regulation and the underlying mechanisms controlling its nucleic acid binding and catalytic activities remain diffusely characterized due to a lack of detailed molecular characterization of Sen1 RNA/DNA and protein-protein interaction interfaces.

Precisely how Sen1 translocates along RNA or DNA, recognizes, unwinds RNA-DNA and DNA-DNA hetero duplexes, and how Sen1 is regulated remains undefined. Here, we report biochemical and structural characterization of *Chaetomium thermophilum* Sen1 (CtSen1). Our results reveal the enzyme motor core is flexibly linked to a dynamically bound helical repeat regulatory domain. We define key elements of the Sen1 catalytic mechanism, and an unexpected mode of *in cis* autoinhibition characterized by potential allosteric control of the enzyme–nucleic acid binding surface.

RESULTS

Cryo-EM Structure of Sen1^{FL}

We employed a selectable high yield YFP-fusion expression approach[26] to express and purify the full-length CtSen1 (Sen1^{FL}, aa 1-1993) in mammalian HEK293F cells (Supplementary Figure 1A). CtSen1 contains the conserved Sen1N domain and SF1B helicase motor core, but like some other fungal species[15], lacks Nrd1-interaction motifs (NIMs). This expression system yields milligram quantities of pure protein suitable for biophysical analysis (Supplementary Figure 1B). Limited tryptic digestion of Sen1^{FL} yields two structurally ordered halves corresponding to the N-terminal domain (Sen1^{Sen1N}), and carboxyl-terminal helicase core (Sen1^{Hel}) (Supplementary Figure 1C). By contrast, a central intrinsically disordered region (IDR) of low-complexity sequence was proteolytically labile, consistent with protein order-disorder predictions (Supplementary Figure 1D).

To understand the basis for Sen1 catalytic activities and regulation we examined its molecular architecture using cryo-electron microscopy (cryo-EM) and determined its structure to 7.4 Å (4.6 Å masked FSC). 2D class averages for Sen1^{FL} revealed a highly asymmetric and elongated architecture resembling the sideview of an inchworm (Figures 1A, Supplementary Figure 2, and Table 1). Overall, the Sen1^{FL} structure is characterized by a prominent protruding Sen1^{Sen1N} helical repeat region that is comprised of 46 α-helices (Figure 1B and 1C, Supplementary Figure 4). The ordered Sen1^{Sen1N} domain in the cryo-EM reconstruction corresponds to the N-terminal 900 residues of the protein. A ~180 amino acid linker (aa 901-1080) between the structured domains is not visible and is likely disordered as expected from our proteolysis results. The three-lobed Sen1^{Hel} nucleic acid motor is bound to the convex face of the helical repeat and is defined by its two closely juxtaposed RecA homology domains (RecA1 and RecA2) (Figure 1C). Two RecA1 insertions include the β-barrel (1b) and helical "Prong" (1c) that are also found in the Upf1[27] and Ighmbp2[28] helicases. An extended interface between Sen1^{Sen1N} and Sen1^{Hel} involves eight Sen1^{Sen1N} helical repeats and both the RecA1 core, and its 1b and 1c insertions. An additional Sen1-specific coiled-coiled (leucine-zipper) insertion extends from the 1c-Prong and engages the Sen1^{Sen1N} helical repeats (Figure 1C). We refer to this element as the leucine-zipper-zipper (LZZ), as it appears to “zipper" up the helical repeat helices, thereby reinforcing the Sen1^{Sen1N}-Sen1^{Hel} juncture.

Sen1^{Hel} is regulated by Sen1^{Sen1N}

We next evaluated CtSen1 catalytic activity using an RNA-DNA helicase assay that monitors Sen1 displacement of black hole quencher (BHQ) modified 44 nucleotide (nt) RNA strand paired to a 5′-FAM labeled 19 nt DNA in the presence of an unlabeled 19 nt trap (Figure 2A). Sen1^{FL} had a rate of RNA/DNA unwinding (k_{obs}) of 0.25 ± 0.01 min^{-1}. By comparison, purified Sen1^{Hel} domain had a 6.8-fold higher activity (k_{obs} = 1.70 ± 0.03 min^{-1}). Together with the proteolysis data, these results suggest that Sen1^{Sen1N} is physically tethered to Sen1^{Hel} via a flexible linker peptide, and that Sen1^{Sen1N} negatively regulates Sen1^{Hel} helicase activity *in cis*. Consistent with this notion, from our inspection of the micrographs, 2D classifications, and ab initio reconstructions, in addition to a full-length enzyme assembly (Figure 1C), two additional species were also prominent in our ab initio

EM reconstructions (Supplementary Figure 2). One of these structures may correspond the helicase core of the protein, but the lack of discernable secondary structure in these envelopes could not allow us to conclusively model this species as the catalytic core. However, we also determined and refined a Sen1^{Sen1N} envelope to 6.9 Å (4.5 Å masked FSC) (Supplementary Figures 2D and 2F). In this structure, the overall fold for Sen1^{Sen1N} is maintained as observed in the full-length reconstruction, but the helicase domain is absent. Together, limited protease digestion, disorder predictions, helicase activity measurements, and EM observations suggest that Sen1^{Sen1N} reversibly engages Sen1^{Hel}, and that deletion of the Sen1^{Sen1N} domain activates the enzyme.

Sen1^{Hel} RNA binding mechanism

To better define the basis for Sen1 substrate engagement we tested Sen1^{FL} and Sen1^{Hel} association with RNA-DNA hybrid substrates bearing increasing 5′-RNA overhangs using electrophoretic mobility shift assays (EMSAs) (Supplementary Figures 3A-3B). Both proteins bound a 44 nt ssRNA, whereas binding of RNA-DNA hybrids requires a minimal flanking 5′-RNA overhang of 10-15 nt, consistent with the known 5′-3′ polarity of Sen1 homologs[25] (Supplementary Figure 3B). Also, like ScSen1, CtSen1 also harbors both DNA-DNA and RNA-DNA unwinding activity (Supplementary Figure 3C). In a gel-based helicase assay monitoring transfer of a labeled DNA strand from an RNA-DNA to a smaller DNA-DNA trap, we tested the RNA length requirement for Sen1 RNA-dependent DNA unwinding activity (Figure 2B). Sen1^{Hel} also displays a strong preference for unwinding RNA-DNA substrates with greater than or equal to a 10 nt 5′ RNA overhang flanking the RNA-DNA heteroduplex. These helicase activity and RNA binding data map an activated catalytic core of the protein Sen1^{Hel} and indicate that stable RNA binding and robust RNA-DNA duplex unwinding requires a nucleic acid binding footprint of greater than or equal to 10 nt of 5′-overhanging ssRNA.

We next trapped a Sen1^{Hel} RNA binding and translocation intermediate by varying ssRNA length and various nucleotides (ATP, ADP, AMP-PNP) in crystallization trials. Monoclinic crystals of the activated Sen1^{Hel} core complexed with ADP and a 15 nt ssRNA substrate diffract to 3.0 Å resolution (Figure 2C-D, Table 2). The ssRNA binding groove localizes to the juncture of the RecA1-RecA2-β-barrel interface and accommodates 10 ordered ribonucleotides of the co-crystallized 15 nt poly-uridine (poly-U) substrate. In one molecule of the crystallographic asymmetric unit, ADP and a sulphate (SO_4) ion bind at the RecA1-RecA2 interface. In the second Sen1 polypeptide, the ATP binding pocket is occupied by two sulphate molecules, in a conformation that is overall like the ADP-SO4 bound state. In this later molecule we surmise that as both the P-loop and the γ-phosphate binding site are bound with sulphate anions, that closure of the ATP-binding groove was stabilized during crystallization. For structural discussions we focused our analysis on ADP-SO_4 bound molecule as in this configuration, ADP-SO_4 mimics a hydrolyzed ATP, prior to release of inorganic phosphate[29].

The Sen1^{Hel} RNA binding interface is defined by a basic amino acid and Ser-Thr rich groove that traverses the paired Sen1 RecA homology motor domains (Figure 2E, Supplementary Figure 5). Sen1 utilizes a dual-grip configuration for ssRNA binding, similar

to other helicases[22,30]. Within the 5′ grip, eight conserved residues (R1779, F1788, R1794, Y1734, S1698, T1761, D1763, and T1605) clasp six nucleotides (U1-U6). Contacts to the 5′-terminal end of the substrate kink and wrap the RNA around the distal end of RecA2. In the second grip, the four 3′-terminal nucleotides (U7-U10) are engaged exclusively by the RecA1 core (S1395, T1550, R1427, T1273, T1272, R1276 and H1556) and the RecA1-β-barrel insertion (N1270). A surface electrostatic view shows how Sen1^{Hel} envelops ssRNA utilizing an electropositive RNA binding channel (Figure 2F). Close positioning of the 3′ terminus of ordered RNA next to the 1c-Prong suggests this motif is important for RNA-DNA strand separation during helicase unwinding. In addition, an electropositive surface proximal to the emergence point of the last ordered RNA 3′-nucleobase is appropriately positioned to accommodate the RNA-DNA hybrid that will be unwound as the enzyme translocates in the 5′ to 3′ direction. Consistent with this notion, docking using an RNA-DNA hybrid substrate (from PDB: 2QK9) in HADDOCK[31] identifies possible duplex binding poses at this site (Figure 2G).

The Sen1 RNA translocation power stroke

The SF1B superfamily of 5′-3′ helicases and translocases have been broadly classified into two branches, the Pif1-like subfamily (e.g. Pif1, RecD) and the Upf1-like subfamily to which Sen1/SETX belongs[22]. A great deal of our understanding of SF1B helicases 5′-3′ translocation comes from seminal studies on the Pif1-like enzyme RecD2[32]. Similar to RecD2[32], and the SF1A superfamily enzyme UvrD[33] we hypothesize that ATP dependent motor domain ratcheting drives Sen1 RNA translocation. In this model, alternating nucleic acid grips operates in Sen1 to guide ssRNA binding and RNA translocation via tight and weak ssRNA binding within the RecA1 and RecA2 domains.

Compared to other structurally characterized helicases, Sen1 is most closely related to Upf1[27] and Ighmbp2[28], though it should be noted neither Upf1 nor Ighmbp2 have Sen1N-like N-terminal domains. Structures of Upf1 have been solved bound to non-hydrolyzable AMP-PNP, phosphate, and ADP bound states in the absence of RNA[34]. In addition, a Upf1-RNA-ADP-AlF_4^- transition state mimic has been trapped[27]. A structural overlay of the Sen1-ADP-SO_4 complex with the Upf1-RNA-ADP- AlF_4^- transition state mimic shows how Sen1 has generally similar overall RNA binding characteristics (Figure 3A). The exception to this is the orientation of the β-barrel that in Upf1 in a distinct conformation compared to the Sen1. Separation of the RecA1-RecA2 domains of Sen1 is also greater compared to Upf1, possibly reflecting differences in a transition state mimic versus the post-hydrolyzed ADP-SO_4 state of the Sen1-RNA complex.

To better understand the Sen1 RNA translocation mechanism, we analyzed nucleotide-dependent conformational changes in the enzyme. Structural superposition of our CtSen1-RNA-ADP-SO_4 quaternary complex with a previously determined ScSen1-ADP complex that crystallized in absence of nucleic acid[23] (RCSB PDB 5MZN) reveals elaborate global Sen1^{Hel} conformational changes that stem from local rearrangements in the nucleotide binding site (Figure 3B). In this superposition the RecA1 domains are well aligned overall, but we observe a concerted ~6-8 Å rigid body translation and a −30° rotation of the RecA2 domain relative to the RecA1 core. In the RNA-ADP-SO_4 bound state determined here, the

sulphate ion γ-phosphate mimic acts as a lynchpin that maintains interdomain contacts and is coordinated at the nexus of the RecA1 K1346 (Motif I, P-loop), Q1601 (Motif III), and RecA2 R1640 (Motif IIIa) and R1801 (Motif VI) (Figure 3C and Supplementary Figure 5). By comparison, in the ADP-bound RNA-free state of ScSen1, absence of the γ-phosphate is coincident with the collapse of this interdomain salt-bridging network. Local side chain rearrangements and a global shift in the RecA2 domain are positioned to rachet bound RNA (Figure 3C and 3D). Overall, the conformational differences observed are appropriate to drive a stepwise 1 nt helicase ratcheting during the helicase power stroke by pulling the RecA2 bound 5′-end away from RecA1 and facilitate 5′-3′ RNA translocation coincident with phosphate release. In addition, RecA1 Arg 1427 (Motif 1b) is positioned to serve as a ratchet "pawl" akin to nucleobase stacking interactions observed for mycobacterial AdnAB helicase[35,36] (Figure 2E).

Determinants of Sen1 autoinhibition

As the Sen1^{Sen1N} domain negatively regulates catalytic activity of the full-length protein (Figure 2A), we hypothesized the full-length structure characterized here reflects an auto-inhibited state of the enzyme. We further reasoned that tethering of Sen1^{Sen1N} to the Sen1^{Hel} domain via a flexible linker facilitates reversible binding of the Sen1N domain to the helicase core (Figures 4A and 4B). To evaluate regulatory roles of the Sen1^{Sen1N} and the IDR linker, we engineered a Sen1 internal truncation (Sen1$^{N\text{-}PP\text{-}C}$) that replaces the native ~180 amino acid linker with a tandem PreScission-protease cleavable tether (Figure 4A-C). This design is facilitated by the close juxtaposition of the C-terminal end of Sen1^{Sen1N} and the N-terminal flank of Sen1^{Hel}. Absent nucleic acid, Sen1^{Hel} harbors no detectable ATPase activity under the conditions examined (Supplementary Figure 3D). However, the addition of 30 nt ssRNA (30U) 44 nt ssRNA (44U) (but not 15 nt ssRNA, 15U) all stimulated Sen1 ATPase hydrolysis (Supplementary Figure 3D, Supplementary Table 2). Likewise, a helicase substrate RNA-DNA hybrid stimulates ATPase activity as expected (Figure 4D). Strikingly, truncation of the linker results in marked attenuation of Sen1 nucleic acid stimulated ATPase (Figure 4D) and RNA-DNA unwinding activities (Figures 4E and 4F) compared to Sen1^{FL} or Sen1^{Hel}. However, Sen1$^{N\text{-}PP\text{-}C}$ autoinhibition is reversible, as protease cleavage liberates the catalytic domain from Sen1^{Sen1N} as engineered (Figure 4C), and partially restores ATPase and helicase activities (Figures 4D-F). Thus, covalent tethering of Sen1^{Sen1N} facilitates robust Sen1 autoinhibition. Moreover, interdomain linker length is tuned for reversible suppression of Sen1 helicase and ATPase activities as shortening of the linker length results in robust autoinhibition.

A detailed analysis of enzyme conformational changes associated with auto-inhibition was initially precluded as the resolution of our Sen1^{FL} reconstruction was limited (Supplementary Figure 2). We reasoned that the Sen1$^{N\text{-}PP\text{-}C}$ internal deletion construct might also be of utility in structural determination of the autoinhibited state given this construct is strongly autoinhibited. Indeed Sen1$^{N\text{-}PP\text{-}C}$ particles yielded a 3.69 Å (3.17 Å masked FSC) cryo-EM map suitable for tracing the Sen1 polypeptide, in the presence of ADP (Figure 5A, Supplementary Figure 6). The Sen1$^{N\text{-}PP\text{-}C}$ structure shows how a 3-point contact of the Sen1^{Sen1N} domain stabilizes an inhibited conformation of Sen1^{Hel}. The three Sen1^{Sen1N}- Sen1^{Hel} interaction interfaces (Int1-Int3, Figure 5B) contribute to an extensive

(2686 Å^2 buried solvent accessible surface) interaction interface between the domains. An analysis of the conservation of the Sen1^{Sen1N} domain surface from 39 Sen1 homologs using ConSurf[37] shows how the Int1-Int3 surfaces on the helical repeat that are utilized for Sen1^{Hel} engagement all correspond to conserved regions of the protein (Figure 5C). A major feature of the Sen1^{Hel}-Sen1^{Sen1N} interaction interface is the extended LZZ RecA1 insertion (aa 1457-1525) that binds to the Sen1^{Sen1N} helical array at Int1 (Figure 5B, Supplementary Figure 4 and Supplementary Figure 5). Several complimentary salt bridging interactions are formed from LZZ helix α59 to the Sen1^{Sen1N} domain helices α30, α32 and α35 (Figure 5D). Int2 involves a direct interaction with the Sen1 β-barrel (1b) insertion and is composed of a mixture of salt bridging interactions (e.g. R718 to E1188) and hydrophobic interactions (Figure 5E). A core conserved element of Int2 is a short helical element initiated by P712 that binds in a shallow pocket on the β-barrel domain. Like Int1, Int3 involves the 1c-prong-LZZ binding (α60) from the helicase domain via a series of complementary salt bridges with the Sen1^{Sen1N} helical repeat (α41 and α43) (Figure 5F). Overall, the inter-domain interactions are mediated by an array reversible salt-bridging contacts that secure the catalytic domain in a conformation that appears incompatible with RNA-DNA substrate engagement.

To directly test functional roles of the Sen1^{Sen1N}-Sen1^{Hel} interface, we probed interactions between Sen1^{Sen1N} and the Sen1^{Hel} helicase core. C-terminally hemagglutinin-tagged helicase domain (c-HA-Sen1^{Hel}) bound to column immobilized MBP-Sen1^{Sen1N}, but not to MBP controls (Figure 5G). However, a Sen1^{Hel} mutant with an internal deletion mutation within the LZZ (Sen1^{Hel}-ΔLZZ, Δ1457-1525, Figure 5H) that deletes all Int1 interdomain contacts and a portion of helicase domain residues participating in Int3 fails to bind Sen1^{Sen1N}, consistent with a critical role for the LZZ in mediating the interdomain interaction. Given the direct interaction between regulatory and catalytic domains, we next tested if Sen1^{Sen1N} can modulate Sen1^{Hel} helicase activity *in trans*. Titration of purified Sen1^{Sen1N} suppresses Sen1^{Hel} unwinding activity to ~25% of WT at 800 nM Sen1^{Sen1N} (Figure 5H). Furthermore, deletion of the LZZ does not impair helicase activity, but renders the catalytic core immune to Sen1^{Sen1N} mediated auto-inhibition *in trans*. Thus, we conclude that direct binding of the Sen1^{Sen1N} to the catalytic core is stabilized by the LZZ, and that the LZZ facilitates autoinhibition.

Sen1^{Sen1N} regulates Sen1^{Hel} substrate engagement

To better understand the mechanism of helicase regulation, we examined structural superpositions of the autoinhibited Sen1$^{N\text{-}PP\text{-}C}$–ADP structure with the Sen1^{Hel}–RNA–ADP complex. A morph between these two states reveals a complex cascade of rearrangements in Sen1^{Hel} that is coincident with Sen1^{Sen1N} binding (Supplementary Movie 1). The salient features of this transition include: 1) LZZ “zippering” of the Sen1^{Sen1N} domain and conformational change of the LZZ upon binding Sen1^{Sen1N}, 2) Wedging of the Sen1^{Sen1N} domain between the RecA1 β-barrel and RecA1 core domain junction, and 3) Closure of the RNA binding channel (Figure 6A). In the RNA bound crystal structure, the LZZ insertion is ordered for the two molecules in the asymmetric unit but stabilized by crystal contacts. Compared to the RNA bound state, the LZZ undergoes significant reorganization when engaged with Sen1^{Sen1N}, consistent with the key role for the LZZ in stabilizing Sen1^{Hel}–

Sen1^{Sen1N} interactions (Figure 6A). Sen1^{Sen1N} wedging pushes the β-barrel towards the RNA binding channel. Coincident with this motion, an array of conformational changes are associated with complete rearrangement of the RNA binding cleft. Visualization of the Sen1 molecular surface shows how the ssRNA binding channel is completely blocked in the Sen1$^{N\text{-}PP\text{-}C}$-ADP complex structure (Figures 6B and 6C). Structural comparisons of the RNA-bound and inhibited state indicates that blockage of the RNA binding channel is achieved by a series of conformational changes in the RNA binding loops that reorganize to engage the β-barrel, and sterically occlude the ssRNA substrate binding cleft.

To test if autoinhibition regulates substrate binding, we compared equilibrium substrate binding of Sen1^{Hel} and Sen1$^{N\text{-}PP\text{-}C}$ to a 40 nt ssRNA using fluorescence polarization (FP) (Figure 6D). Consistent with the structural observations, RNA binding was significantly impaired in the autoinhibited Sen1$^{N\text{-}PP\text{-}C}$ protein construct (Figure 6D), but only in the presence of ADP nucleotide. In the absence of nucleotide, Sen1$^{N\text{-}PP\text{-}C}$ binds ~2-fold more strongly than the isolated helicase domain to a 40 nt ssRNA. We speculate that the Sen1N bound catalytic domain can bind to a short ssRNA, by engaging an opened RNA binding cleft. Overall, our structural and biochemical results show that direct interactions of the Sen1^{Sen1N} with Sen1^{Hel} suppresses RNA/DNA dependent ATPase and RNA-DNA unwinding activity of Sen1^{Hel} and reveal that autoregulation of the enzyme involves dynamic intramolecular binding of Sen1^{Hel} to Sen1^{Sen1N} that stabilizes nucleotide dependent states which are incompatible with RNA substrate engagement. Interestingly, we also note that a proposed RNA-DNA hybrid binding site determined by nucleic acid docking (Figure 2G) overlaps completely Sen1^{Sen1N} domain in the autoinhibited state, suggesting that Sen1^{Sen1N} might also compete directly with RNA-DNA substrate binding by mimicking the heteroduplex region of an RNA-DNA hybrid (Figure 6E).

AOA2 mutants impair Sen1 RNA binding and helicase activity

We analyzed human AOA2 catalytic core mutants in the context of the CtSen1^{Hel}-RNA complex structure (Figure 7, Supplementary Figure 4, and Supplementary Table 1). An AlphaFold model[38] of the hSETX catalytic core shows close similarity to our CtSen1-RNA complex structure (Figure 7A). We used both structures to make predictions of the potential impacts of *SETX* missense variants (Figure 7B, Supplementary Table 1). Many of the mutations (F1756S, A1945P, L1976R, L1977F, N2037D, I2179S, H2197R, M2229T, I2264M, I2386T, R2444H, R2444C) would be predicted to impact protein folding. Several mutants map directly to the ssRNA binding region or proximal to structural elements contacting ssRNA (P1805S, C2006Y, L2155W, N2010S, P2213L, T2373P) or the predicted RNA/DNA hybrid binding site near the base of the LZZ (R2136H, R2136C). A third class of mutations are found close to the ATP binding site, and therefore may impact ATP binding and/or hydrolysis (D2207V, R2414Q). Given the proximity to the RecA1-RecA2 interface and their participation in structural salt bridging interactions close to the ATP binding site, 5 substitutions (R2380T, R2380W, R2380G, R2380Q, K2382E), might impact protein folding and/or ATP regulated conformational changes. Lastly, two mutations cluster to a surface on the RecA2 domain and may mark a protein binding surface of unknown function (F2363L, P2368R).

Our attention focused on two mutations that map to the RNA binding cleft characterized here. P1805S (L1203S in CtSen1) and L2155W (L1551W in CtSen1) mutations directly flank the structurally characterized RNA binding channel (Figure 7C). In FP ssRNA binding assays using a FAM-labeled substrate, compared to WT Sen1^{Hel} (K_d= 310 nM), Sen1^{Hel}-L1203S (K_d= 420 nM) had a modest impact on substrate equilibrium binding (Figure 7D). By comparison, the L1551W substitution that we would predict to distort the base of the ssRNA binding cleft bound ssRNA weakly (K_d=1350 nM) (Figure 7D). We find that both mutations impair substrate stimulated ATPase activity (Figure 7E), and that the L1551W mutant has a severe impact on RNA-DNA unwinding activity (Figure 7F). Thus, we conclude that the integrity of the ssRNA binding cleft characterized here is compromised in a subset of AOA2 mutations linked to neurodegenerative disease.

DISCUSSION

Herein, we define the global architecture of the Sen1 RNA-DNA helicase. Our results establish that interactions of Sen1^{Sen1N} with Sen1^{Hel} regulates helicase activity *in cis* (Figure 7H). The N-terminal helical autoregulatory domain directly engages the Sen1 catalytic core through extensive molecular interactions. Sen1^{Sen1N} deletion activates the protein *in vitro*, and the Sen1^{Sen1N} helical repeats suppress Sen1 catalytic activity through nucleotide dependent allosteric regulation of the helicase RNA-DNA hybrid binding channel. This regulatory mechanism involves both modulation of ATPase activity and RNA binding and translocation, with the major effect being on the later. It is also probable that Sen1^{Sen1N} binding to Sen1^{Hel} restricts the interdomain motions regulated by ATP-induced conformational changes, thereby rendering the catalytic core arthritic, preventing molecular motions that underpin the Sen1 RNA-DNA unwinding chemistry. A critical feature of this interaction is flexible tethering of Sen1^{Sen1N} to Sen1^{Hel}, and the length of the intrinsically disordered tether is an important regulator of helicase inhibition. The IDR region is comprised of “low complexity” sequence and predicted to be disordered (Supplementary Figure 1D). Notably, there are stretches of conserved sequences present in the IDR. In addition to serving as a flexible regulatory tether, the interdomain linker might also be directly involved in regulating enzyme activation by binding regulatory partners, or to nucleic acid directly.

Our Sen1 structures also provide insights into Sen1 mutations mapping to the N-terminal domain that impact protein-protein interaction and have pleiotropic effects on Sen1 transcriptional regulation and gene expression. The Sen1-K128E substitution blocks interaction with Rnt1p ribonuclease and Sen1-R302W impairs binding to Rbp1p, the large subunit of yeast RNA polymerase II[39]. Sen1-K128E and Sen1-R302W variants differentially affect Sen1 functions in RNA processing and transcription respectively[39]. An additional *sen1-3* allele Sen1^{Sen1N} triple mutation (W773A, E774A, W777A) most likely disrupts Sen1^{Sen1N} protein folding and specifically impacts Sen1 recruitment to the DNA replisome and protein-protein interactions with Ctf4 and Mrc1[19]. Thus, the collective data point to a complex regulatory role for the Sen1N region in regulating protein-protein interactions and modulating Sen1 catalytic activity. We hypothesize that Sen1^{Sen1N} interactions with protein partners such as RNA polymerase or Ctf4 facilitate both Sen1 recruitment to RNA-DNA targets, and regulation of Sen1 catalytic activities. That the majority of autoinhibitory

contacts from the Sen1N domain are assembled by salt-bridging networks is consistent with a role for these interactions in mediating a reversible regulatory switch. Consistent with this hypothesis the equivalent region to the CtSen1 LZZ is important for mediating yeast Sen1 transcriptional termination activity and interaction with RNA polymerase[23]. Thus, the Sen1^{Sen1N} and Sen1^{Hel} domain surfaces participating in autoinhibition are likely involved in regulating transition to the active helicase state depending on protein binding partner context. Sen1 is most like the nonsense mediated decay Upf1 RNA helicase. With respect to the autoregulatory mechanism, in Upf1, an N-terminal CH domain dynamically regulates activity of the core helicase domain in concert with the trans binding factor Upf2[27,40]. We posit that Sen1^{Sen1N} binding factors recruit Sen1 to RNA-DNA hybrids and may regulate Sen1^{Sen1N}- helicase dynamics.

The X-ray structures of the Sen1 catalytic core further reveal conserved determinants for its RNA binding and translocation mechanism. Like other nucleic acid helicases[22,33], the Sen1 helicase mechanism involves conformational changes governed by ATP binding and hydrolysis, as well as dynamic remodeling of the RNA-DNA binding surface. While the ssRNA binding site is well defined in our crystal structures, it remains an open question as to how the enzyme engages the duplex portion of the substrate. Docking analysis suggests that a suitable site for RNA-DNA hybrid engagement is found on the β-barrel SF1B insertion. The positioning of this site is conspicuous as it directly overlaps with the Sen1^{Sen1N} binding site on the catalytic domain observed in the autoinhibited conformation. Thus, we hypothesize that helicase regulation also involves direct mimicry of the nucleic acid binding surface by Sen1^{Sen1N}. Like budding yeast Sen1, *Ct*Sen1 also unwinds both RNA-DNA and DNA-DNA duplexes. Consistent with these observations, inspection of the Sen1-RNA complex structure reveals that no specific protein-nucleic acid contacts appear suited to differentiate RNA from DNA. Sen1 DNA helicase activity may be relevant to DNA replication and repair roles for Sen1 homologs, consistent with recruitment of the protein into DNA replication and repair machineries[8,9,19]. More work is needed to assess the structural and multifunctional roles for Sen1 RNA-DNA and DNA-DNA unwinding activities.

Limitations of this study

There are limitations to the current study. It is possible that regulation of vertebrate SETX via the N-terminal domain is conserved with Sen1. However, the inability to produce suitable quantities of full-length human SETX has precluded detailed analysis of the conservation of this mechanism to date. In our analysis of ATP-dependent conformational control of Sen1 function we have inferred mechanism using states from two different species captured in different crystalline states. Additional work is required to further characterize the nature of Sen1 interactions with regulatory factors, to decipher the basis for additional Sen1 and vertebrate SETX RNA-DNA and DNA-DNA unwinding reaction and ATP-dependent translocation intermediates, and to define the impacts of AOA2 and ALS4 mutations on these RNA-DNA transactions.

STAR Methods

RESOURCE AVAILABILITY

Lead Contact—Further information and requests for resources and reagents should be directed to and will be fulfilled by the Lead Contact, R. Scott Williams (williamsrs@niehs.nih.gov).

Materials Availability—All materials generated by this study are listed in the Key Resources table and are available from the Lead Contact without restriction.

Data and Code Availability

- The data presented in this paper will be shared by the lead contact upon request. Uncropped gels are available at Mendeley at doi:10.17632/djm6wdc5tg.1. Cryo-EM maps have been deposited in the Electron Microscopy Data Bank (EMDB). X-ray data and refined molecular models have been deposited in the RSCB Protein Data Bank (PDB). EMDB and PDB Accession codes are available in the key resources table. All datasets will be publicly accessible at the date of publication.
- This paper does not report original code.
- Any additional information required to reanalyze the data reported in this paper is available from the lead contact upon request.

Experimental Model and Study Participant Details Bacterial strain—BL21-AI cells (Life Technologies) were transformed with the constructs for protein expression overnight at 15°C in Terrific Broth. Induction of expression was carried out by the primary addition of 0.1% (w/v) final concentration L-Arabinose (GoldBio).

Mammalian cell lines—HEK 293 Freestyle (HEK293F) cells were used to express YFP fusion full length Sen1 proteins. Stable cell lines were created by Lipofectamine 2000 (Thermo Fisher) followed by rounds of blasticidin selection.

METHOD DETAILS

***Chaetomium thermophilum* Sen1 construct designs—**The Chaetomium thermophilum Sen1 homolog CtSen1^{FL} (UniProt G0S163_CHATD), CtSen1^{Sen1N} (aa 1-900), CtSen1^{Hel} (aa 1080-1890), Sen1$^{Hel\text{-}\Delta LZZ}$ (aa 1080-(Δ1457-1525)-1890), and CtSen1$^{N\text{-}PP\text{-}C}$ (CtSen1 aa 1-900-LEVLFQGPLEVLFQGP-1080-1868) were all ordered from Genewiz/Azentra as synthetic genes in pUC57-Kan vector. The synthetic plasmids were designed to contain a Tobacco Etch Virus (TEV) recognition site directly upstream of the gene and the entirety was flanked by AttL recombination sites for LR subcloning into Gateway destination vectors for expression as N-terminally-tagged fusion proteins. CtSen1^{FL} and CtSen1$^{N\text{-}PP\text{-}C}$ were codon optimized for mammalian expression and subcloned into the ampicillin resistant (Amp^{R}) plasmid pcDNA6.2 N-EmGFP-DEST (Invitrogen). CtSen1^{Sen1N}, CtSen1^{Hel}, Sen1$^{Hel\text{-}\Delta LZZ}$ were codon optimized for bacterial expression and subcloned into pDEST-His-MBP (Amp^{R}, Addgene). All plasmids were

confirmed by DNA sequencing (Genewiz/Azentra). QuikChange site-directed mutagenesis (Stratagene) was used to create the crystallization construct CtSen1$^{Hel\text{-}1878}$, the CtSen1^{Hel} mutants L1203S and L1551W, and the CtSen1^{Hel} and CtSen1$^{Hel\text{-}\Delta LZZ}$ C-terminal-HA fusions.

Protein expression and purification—HEK293F cells stably overexpressing N-terminal YFP fusion proteins, CtSen1^{FL} and CtSen1$^{N\text{-}PP\text{-}C}$, were created by Lipofectamine 2000 (Thermo Fisher) transfection followed by rounds of blasticidin selection. Protein was isolated from suspension culture via anti-GFP/YFP single domain camelid nanobody (sdAB) as previously described[26] and released from the nanobody by on-column TEV protease digestion in Sen1 storage buffer (20 mM Tris pH 7.9, 200 mM NaCl, 2 mM $MgCl_2$, 1 mM TCEP). Protein was further purified by size-exclusion chromatography in Sen1 storage buffer followed by high resolution anion exchange chromatography on a Cytiva MonoQ 10/100GL column in ion exchange buffers (Buffer A: 20 mM Tris pH 7.9, 1 mM TCEP and Buffer B: 20 mM Tris pH 7.9, 1 M NaCl, 1 mM TCEP). Sen1^{FL} elutes at ~140 mM NaCl. Protein was then buffer exchanged into Sen1 storage buffer using Millipore spin 10,000 MW cutoff concentrators. For experiments where CtSen1$^{N\text{-}PP\text{-}C}$ was digested with PreScission protease (GE Healthcare/Cytiva) to yield separate N-terminal and C-terminal domains, 1 μL of 0.8 mg mL^{-1} protease was added to 15 μL of 2 mg mL^{-1} protein and incubated for 1 hour at room temperature.

CtSen1^{Sen1N}, CtSen1^{Hel}, CtSen1^{Hel}L1203S, CtSen1^{Hel}L1551W, CtSen1$^{Hel\text{-}1878}$, and Sen1$^{Hel\text{-}\Delta LZZ}$ proteins were expressed as N-terminal His-MBP fusions. BL21-AI cells were transformed with constructs for protein expression overnight at 15°C in Terrific Broth. Induction of expression was carried out by the primary addition of 0.1% (w/v) final concentration L-Arabinose. Following amylose affinity chromatography performed in Sen1 storage buffer for binding and (plus 30 mM maltose) for protein elution, proteins were subjected to overnight TEV protease digestion for MBP tag removal prior to ion exchange chromatography in ion exchange buffers (see above). For pull-down assays using MBP-CtSen1^{Sen1N}, TEV digestion was omitted. CtSen1^{Hel} constructs and mutants were purified by cation exchange chromatography (Cytiva HiTrap SP column) in Buffer A and Buffer B, described above and polished by gel filtration (Cytiva Superdex 200 Analytical 10/300 GL) in Sen1 storage buffer. CtSen1^{Sen1N} constructs, both MBP-tagged and TEV digested, were purified by anion exchange chromatography (Cytiva HiTrap Q column) and polished by gel filtration as described for the CtSen1^{Hel} proteins. Final purity was assessed by SDS-PAGE and fractions pooled and concentrated for subsequent experiments.

Limited proteolysis—CtSen1^{FL} was subjected to limited proteolysis, on ice, in 10 mL reactions containing 1 mg mL^{-1} CtSen1^{FL} combined with 1 mg mL^{-1}, 0.1 mg mL^{-1} or 0.01 mg mL^{-1} trypsin. Reactions were quenched at 5, 15, 30, or 60 minutes by the addition of 2 mM PMSF and Laemmli SDS-PAGE dye followed by incubation at 95°C for 10 minutes. Trypsinized protein was resolved by SDS-PAGE and individual bands excised for peptide identification by LC-MS/MS spectrophotometry. Gel bands were digested using a Progest robotic digester (Genomic Solutions, Ann Arbor, WI). Minced gel bands were incubated twice for 15 min in 100 μL of 25 mM ammonium bicarbonate/50% (v/v) acetonitrile. The

gel was then dehydrated by a 20-min incubation in 100 μL of acetonitrile followed by drying under a nitrogen stream. Then, 270 ng of trypsin (Promega) was added followed by an 8 min incubation at 37 °C. The supernatants from the digests were collected and the gel was re-extracted three times: once with 50 μL of water for 20 min and twice with 20-min incubations in 50 μL of 5% (v/v) formic acid/50% (v/v) acetonitrile. All of these extractions were pooled, lyophilized, and resuspended in 10 μL of 1:1 water with 0.1% formic acid:acetonitrile with 0.1% formic acid. Samples were spotted (0.3 μL) onto a stainless-steel target. A 33% saturated solution of alpha-cyano-hydroxycinnamic acid in 50:50 (v/v) 0.1% formic acid: 0.1% formic acid in acetonitrile was added (0.7 μL) to the sample and mixed on target. MALDI-TOF and MALDI-TOF/TOF (top 6 ions selected for MS/MS) experiments were performed on an Applied Biosystems 4800 Plus MALDI TOF/TOF Analyzer in positive ion reflector modes. The MS was first calibrated externally using the Bruker Daltonics Peptide Calibration Mixture and the MS/MS calibrated externally using the fragment ions of the angiotensin I M+Sen ion (m/z 1298.68). If detected in the sample, autolytic tryptic peaks were used for further internal calibration in the MS mode. A focus mass of m/z 1600 was used for the MS acquisitions. For MS/MS 1000 kV was used for the collision energy. Data were processed and searched inside the Protein Pilot software using a MASCOT search engine. Searches were against the Swiss-Prot/UniProt database and search parameters included tryptic enzyme specificity with up to 2 missed cleavages, 0.06 Da mass tolerance for the MS and a 0.1 Da mass tolerance for the MS/MS, and variable methionine oxidation.

MBP pull-down assays—In Micro Bio-Spin columns (Bio-Rad) 200 μL reactions were assembled with 1 μM of indicated MBP-CtSen1^{Sen1N} fusion or MBP protein in binding buffer (10 mM HEPES pH 7.5, 20 mM NaCl, 0.5 mM TCEP, 0.1 mg ml^{-1} BSA), 1 μM of CtSen1^{Hel}-c-HA or 1 μM of Sen1$^{Hel\text{-}\Delta LZZ}$-c-HA was added followed by 20 μL of amylose resin (NEB). Reactions were mixed on a nutator at 4°C overnight, centrifuged at 1000 x g for 1 min, washed with 100 μL binding buffer, eluted with 20 μL of 50 mM maltose. Samples were resolved on a NuPage (Thermo Fisher) 4–12% Bis–Tris SDS-PAGE followed by immunoblotting with probes for MBP and HA (GeneTex).

Fluorescence polarization RNA Binding Assay—CtSen1 RNA binding was monitored using the change in fluorescence polarization (FP) of a 5'-FAM-labeled single stranded RNA oligonucleotide (Supplementary Table 2). In a 50 μL reaction, 10 nM of labeled RNA substrate was mixed with CtSen1^{Hel} protein at concentrations ranging from 0.01 μM to 10 μM in binding buffer (20 mM HEPES pH 7.5, 50 mM NaCl, 1 mM TCEP, 0.2 mg mL^{-1} BSA, 10% glycerol). Binding reactions were incubated in black, flat bottom, half-area 96 well plates (Corning Costar) for 20 minutes at room temperature, and FP measurements were collected at room temperature with the POLARstar Omega microplate reader (BMG Labtech) using excitation and emission wavelengths of 485 and 520 nm, respectively. Equilibrium binding dissociation constants (K_d) for the RNA interactions were calculated by fitting data expressed as a fraction bound ratio from FP measurements, using the “specific binding with Hill slope” model in GraphPad Prism.

Preparation of CtSen1^{FL} and CtSen1$^{N\text{-}PP\text{-}C}$ cryo-EM specimens—Purified CtSen1^{FL} and CtSen1$^{N\text{-}PP\text{-}C}$ were resolved over a Source Q high resolution anion exchange column (Cytiva) followed by buffer exchange into Sen1 storage buffer. For CtSen1^{FL} sample preparation, protein was concentrated to 1.1 mg mL^{-1} and deposited onto CF-1.2/1.3-3CU-50 C-Flat™ grids (Protochips Inc.) after glow discharging (30 sec, 15 mA) both sides of the grids using a Pelco EasiGlow. 3 μL of Sen1 storage buffer was deposited on the back side of the grid followed by 3 μL of sample on the front side. Grids were plunge-frozen in liquid ethane using the Vitrobot (FEI) plunge-freeze device at 95% relative humidity, chamber temperature 12°C. For CtSen1$^{N\text{-}PP\text{-}C}$ sample preparation, 5 mM ADP was included in the 0.2 mg mL^{-1} protein solution. UltrAuFoil R1.2/1.3 300 mesh gold grids (Quantifoil) were rendered hydrophilic using the Tergeo plasma cleaner (Pie Scientific) and 3 μL protein-ADP sample were deposited onto the grids and blotted for 3 seconds using an Automatic Plunge Freezer (Leica).

Cryo-EM data collection, processing and model building of CtSen1^{FL}—Grids of CtSen1^{FL} were imaged using an FEI Titan Krios transmission electron microscope operating at 300 kV equipped with a K2 summit direct electron detector 130,000 x magnification to a final pixel size of 0.53 Å/pixel using SerialEM 3.7 data collection software. Movies were recorded in counting mode at 130,000 x magnification (Table 1). Motion and drift corrections were performed using MotionCor2[41]. Cryo-EM data processing including CTF corrections were performed in CryoSparc v2.7[42,43]. Following initial automated particle picking and 2D classification, a TOPAZ[44] neural network model facilitated acquisition of high-quality particles for downstream analysis (Supplementary Figure 2A). 2D classifications and ab initio modeling provided three low-resolution volumes that were used as input maps for CryoSparc heterogenous refinement. These volumes corresponded to Sen1^{FL}, Sen1^{Sen1N} and possibly Sen1^{Hel}. Additional rounds of 2D classification ab initio reconstruction and heterogenous refinement in CryoSparc, followed by a final non-uniform refinement yielded a 4.6 Å (masked) resolution cryo-EM reconstruction of Sen1^{FL} (Figure 1A-1C, Supplementary Figure 2C and 2E, and Methods). A second volume class corresponding to Sen1^{Sen1N} was also refined to 4.5 Å (masked) (Supplementary Figures 2D and 2F), whereas the Sen1^{Hel} was poorly defined, but broadly resembled the Sen1^{Hel} core structure. The Sen1^{FL} cryo-EM map was traced in Coot[45] using AlphaFold model templates[46] for the Sen1^{Sen1N} region (aa 1-900). The refined X-ray structure for the Sen1^{Hel} (below) determined herein was used as an initial model to fit the catalytic core. For Sen1^{Hel}, rigid body refinement indicated that the RecA2 domain is found in an opened conformation compared to the RNA bound X-ray structure. An all polyalanine model was refined using real-space refinement in PHENIX[47] (Table 1).

Cryo-EM data collection, processing and model building of Sen1$^{N\text{-}PP\text{-}C}$—Screening of cryo-EM grids for data collection was conducted using Smartscope[48]. Grids of Sen1$^{N\text{-}PP\text{-}C}$ were imaged on an FEI Titan Krios transmission electron microscope operating at 300 kV using a Gatan 3 Bioquantum detector at 130,000 x magnification to a final pixel size of 0.67Å/pixel using SerialEM 3.7 data collection software. Movies were recorded in counting mode at 130,000 x magnification (Table 1). Motion and drift were corrections were performed using MotionCor2[41]. Cryo-EM data processing including CTF corrections were

performed in CryoSparc v2.7[42,43]. Two datasets (6379 micrographs and 3655 micrographs) were collected from the same grid and combined (Supplementary Figure 6A). Following initial automated particle picking and 2D classification, a TOPAZ[44] neural network model facilitated acquisition of high-quality particles for downstream analysis. 2D classifications, *ab initio* reconstructions, were followed by rounds of heterogenous refinement, and non-uniform refinement in CryoSparc yielded a 3.17 Å map suitable for model building and refinement (Supplementary Figure 6).

The Sen1$^{N\text{-}PP\text{-}C}$ cryo-EM map was traced using AlphaFold model templates[46] for the Sen1^{Sen1N} region. Sen1 residues 1-255 are poorly defined in the Sen1$^{N\text{-}PP\text{-}C}$ cryo-EM map and were not modeled. A polyalanine model was built in Coot for residues 244-333 due to static structural disorder. The map was of sufficiently good quality to trace most of the protein chain of Sen1^{Sen1N} (aa 334-888), and Sen1^{Hel} (aa 1102-1844). Regions of the map that had poorly defined surface loops defined were fit as polyalanine or excluded. No cryo-EM density was observed for the engineered PreScission protease cleavable interdomain linker. Real space refinement performed in PHENIX[47] with iterative model building in Coot[45] produced a final model with good refinement statistics (Table 1).

Crystallization and structure determination of CtSen1$^{Hel\text{-}1878}$—A truncated version of the helicase core (CtSen1$^{Hel\text{-}1878}$, aa 1080-1878) was used for crystallization. Crystals of the CtSen1$^{Hel\text{-}1878}$-RNA-ADP-SO_4 complex were grown using the sitting-drop vapor diffusion method by mixing 200 nL of precipitant with 200 nL of protein mixture (10 mg ml^{-1} CtSen1$^{Hel\text{-}1878}$, 8 mM ADP, 40 μM NaF, 10 nt polyribouridine (10 rU) at 1.5 X molar ratio to protein, in Sen1 storage buffer (see above). Crystals were obtained in 200 mM sodium sulfate and 20% (w/v) PEG3350. Crystals grew overnight at 4°C and were transferred to a cryoprotectant containing 2 mM ADP, 16% PEG3350, 26% (v/v) ethylene glycol, then flash frozen in liquid nitrogen. High-resolution datasets were collected at the Advanced Photon Source on beamline 22-ID. X-ray diffraction data were processed and scaled using HKL2000[49] (Table 2). Initial structures were solved using molecular replacement with the S. cerevisiae Sen1 protein (5MZN). Iterative building in[45] and refined in PHENIX[47] (Table 2).

Electrophoretic mobility shift assays—All oligonucleotides were supplied by Integrated DNA Technologies (Supplementary Table 2). Reactions (10 μL) were performed in a buffer containing 10 mM Tris-HCl pH 7.5 and 50 mM NaCl. 10 nM RNA-DNA substrate (Sub4, Supplementary Tables 4 and 5) was incubated with Sen1^{FL}, Sen1$^{N\text{-}PP\text{-}C}$ and Sen1^{Hel} (50, 150, 500 and 1000 nM) on ice for 15 min. Samples were resolved on 6% TBE gels and FAM-labeled reaction products were scanned at 520 nm on a Typhoon FLA 9000 scanner (GE Healthcare). The bands were quantified using ImageQuant.

ATPase assay—Reactions (50 μL) were performed in a buffer containing 10 mM Tris pH 7.5, 50 mM NaCl, 7.5 μM $ZnCl_2$, 1 mM DTT and 0.1 mg mL^{-1} BSA. Sen1 proteins (5 nM) were incubated with Sub6 (5000 nM) (Supplementary Tables 4 and 5), ATP (1 mM) and $MgCl_2$ (2 mM) for 15 min at 37 °C. Samples were quenched with EDTA (10 mM). The hydrolysis products were detected using colorimetric Malachite Green Phosphate Assay Kit (Cayman). Absorbance was measured at 620 nm. Free phosphate concentrations were

calculated from the calibration curve and used to determine the percentage of hydrolyzed ATP.

RNA-DNA unwinding assays—Reactions were performed in a buffer containing 10 mM Tris pH 7.5, 50 mM NaCl, 7.5 μM $ZnCl_2$, 1 mM DTT and 0.1 mg mL^{-1} BSA. Gel-based unwinding assays were performed in 10 μl reactions containing $Sen1^{Hel}$ (50 nM), Sub1-Sub5 (20 nM) (Supplementary Tables 4 and 5), and 19-Trap DNA (200 nM) used to trap unwound FAM 19-DNA (Supplementary Table 2). Reactions were initiated by addition of a mixture containing ATP (1 mM) and $MgCl_2$ (2 mM) and allowed to proceed for 15 min at 37°C. Reactions were stopped by addition of EDTA (10 mM). Proteins were removed by treatment with SDS (1%) and Proteinase K (0.1 mg mL^{-1}). Samples were resolved on 15% TBE gels and FAM-labeled reaction products were visualized on a Typhoon FLA 9000 scanner (GE Healthcare). For fluorescence-based unwinding assays, the Sub7 was used as RNA-DNA substrate. Reactions were performed in 50 μL reactions in 5 replicates. Enzymes at the indicated concentrations were incubated with 50 nM Sub7 (Supplementary Tables 4 and 5). Reactions were initiated by addition of a mixture containing ATP (1 mM) and $MgCl_2$ (2 mM). The signal was detected at 520 nm every 10 sec over 30 min at room temperature. The initial rates were calculated from the linear fit of the percentage of unwound RNA-DNA during the first 5 min of the reaction. Initial rates were plotted against the amount of enzyme (x-axis). Rates of reactions were calculated from the slope of the curves. For mutational analysis, $Sen1^{Hel}$ mutants (1 nM) were incubated with Sub7 (50 nM) for 10 min at RT.

QUANTIFICATION AND STATISTICAL ANALYSIS

All statistical analysis was performed using GraphPad Prism 8. The test performed, the sample size (n) and the number of independent replicates for each experiment are depicted in the figure legends.

Supplementary Material

Refer to Web version on PubMed Central for supplementary material.

ACKNOWLEDGMENTS

The research was supported by the US National Institute of Health Intramural Program, US National Institute of Environmental Health Sciences (NIEHS) 1Z01ES102765 (to R.S.W.). We thank Dr. Lars Pedersen of the NIEHS Collaborative X-ray Crystallography Group for data collection support and the Advanced Photon Source (APS) Southeast Regional Collaborative Access Team (SER-CAT) for beamline access. Use of the APS was supported by the U. S. Department of Energy, Office of Science, Office of Basic Energy Sciences, under Contract No. W-31-109-Eng-38. We thank Dr. Lars Pedersen and Dr. Robin Stanley for expert comments on the manuscript.

REFERENCES

1. Garcia-Muse T, and Aguilera A (2019). R Loops: From Physiological to Pathological Roles. Cell 179, 604–618. 10.1016/j.cell.2019.08.055. [PubMed: 31607512]
2. Crossley MP, Bocek M, and Cimprich KA (2019). R-Loops as Cellular Regulators and Genomic Threats. Mol Cell 73, 398–411. 10.1016/j.molcel.2019.01.024. [PubMed: 30735654]
3. Groh M, Albulescu LO, Cristini A, and Gromak N (2017). Senataxin: Genome Guardian at the Interface of Transcription and Neurodegeneration. J Mol Biol 429, 3181–3195. 10.1016/j.jmb.2016.10.021. [PubMed: 27771483]

4. Ursic D, Chinchilla K, Finkel JS, and Culbertson MR (2004). Multiple protein/protein and protein/RNA interactions suggest roles for yeast DNA/RNA helicase Sen1p in transcription, transcription-coupled DNA repair and RNA processing. Nucleic Acids Res 32, 2441–2452. [PubMed: 15121901]
5. Steinmetz EJ, Warren CL, Kuehner JN, Panbehi B, Ansari AZ, and Brow DA (2006). Genome-wide distribution of yeast RNA polymerase II and its control by Sen1 helicase. Mol Cell 24, 735–746. [PubMed: 17157256]
6. Suraweera A, Becherel OJ, Chen P, Rundle N, Woods R, Nakamura J, Gatei M, Criscuolo C, Filla A, Chessa L, et al. (2007). Senataxin, defective in ataxia oculomotor apraxia type 2, is involved in the defense against oxidative DNA damage. J Cell Biol 177, 969–979. [PubMed: 17562789]
7. Cohen S, Puget N, Lin YL, Clouaire T, Aguirrebengoa M, Rocher V, Pasero P, Canitrot Y, and Legube G (2018). Senataxin resolves RNA:DNA hybrids forming at DNA double-strand breaks to prevent translocations. Nat Commun 9, 533. 10.1038/s41467-018-02894-w. [PubMed: 29416069]
8. Rawal CC, Zardoni L, Di Terlizzi M, Galati E, Brambati A, Lazzaro F, Liberi G, and Pellicioli A (2020). Senataxin Ortholog Sen1 Limits DNA:RNA Hybrid Accumulation at DNA Double-Strand Breaks to Control End Resection and Repair Fidelity. Cell Rep 31, 107603. 10.1016/j.celrep.2020.107603. [PubMed: 32375052]
9. Yuce O, and West SC (2013). Senataxin, defective in the neurodegenerative disorder ataxia with oculomotor apraxia 2, lies at the interface of transcription and the DNA damage response. Mol Cell Biol 33, 406–417. 10.1128/MCB.01195-12. [PubMed: 23149945]
10. Zardoni L, Nardini E, Brambati A, Lucca C, Choudhary R, Loperfido F, Sabbioneda S, and Liberi G (2021). Elongating RNA polymerase II and RNA:DNA hybrids hinder fork progression and gene expression at sites of head-on replication-transcription collisions. Nucleic Acids Res 49, 12769–12784. 10.1093/nar/gkab1146. [PubMed: 34878142]
11. Moreira MC, Klur S, Watanabe M, Nemeth AH, Le Ber I, Moniz JC, Tranchant C, Aubourg P, Tazir M, Schols L, et al. (2004). Senataxin, the ortholog of a yeast RNA helicase, is mutant in ataxia-ocular apraxia 2. Nat Genet 36, 225–227. [PubMed: 14770181]
12. Lavin MF, Gueven N, and Grattan-Smith P (2008). Defective responses to DNA single- and double-strand breaks in spinocerebellar ataxia. DNA Repair (Amst) 7, 1061–1076. [PubMed: 18467193]
13. Chen X, Muller U, Sundling KE, and Brow DA (2014). Saccharomyces cerevisiae Sen1 as a model for the study of mutations in human Senataxin that elicit cerebellar ataxia. Genetics 198, 577–590. 10.1534/genetics.114.167585. [PubMed: 25116135]
14. Steinmetz EJ, Warren CL, Kuehner JN, Panbehi B, Ansari AZ, and Brow DA (2006). Genome-wide distribution of yeast RNA polymerase II and its control by Sen1 helicase. Mol Cell 24, 735–746. 10.1016/j.molcel.2006.10.023. [PubMed: 17157256]
15. Zhang Y, Chun Y, Buratowski S, and Tong L (2019). Identification of Three Sequence Motifs in the Transcription Termination Factor Sen1 that Mediate Direct Interactions with Nrd1. Structure 27, 1156–1161 e1154. 10.1016/j.str.2019.04.005. [PubMed: 31104813]
16. Thiebaut M, Kisseleva-Romanova E, Rougemaille M, Boulay J, and Libri D (2006). Transcription termination and nuclear degradation of cryptic unstable transcripts: a role for the nrd1-nab3 pathway in genome surveillance. Mol Cell 23, 853–864. 10.1016/j.molcel.2006.07.029. [PubMed: 16973437]
17. Steinmetz EJ, Conrad NK, Brow DA, and Corden JL (2001). RNA-binding protein Nrd1 directs poly(A)-independent 3'-end formation of RNA polymerase II transcripts. Nature 413, 327–331. 10.1038/35095090. [PubMed: 11565036]
18. Porrua O, Hobor F, Boulay J, Kubicek K, D'Aubenton-Carafa Y, Gudipati RK, Stefl R, and Libri D (2012). In vivo SELEX reveals novel sequence and structural determinants of Nrd1-Nab3-Sen1-dependent transcription termination. EMBO J 31, 3935–3948. 10.1038/emboj.2012.237. [PubMed: 23032188]
19. Appanah R, Lones EC, Aiello U, Libri D, and De Piccoli G (2020). Sen1 Is Recruited to Replication Forks via Ctf4 and Mrc1 and Promotes Genome Stability. Cell Rep 30, 2094–2105 e2099. 10.1016/j.celrep.2020.01.087. [PubMed: 32075754]

20. Simon AC, Zhou JC, Perera RL, van Deursen F, Evrin C, Ivanova ME, Kilkenny ML, Renault L, Kjaer S, Matak-Vinkovic D, et al. (2014). A Ctf4 trimer couples the CMG helicase to DNA polymerase alpha in the eukaryotic replisome. Nature 510, 293–297. 10.1038/nature13234. [PubMed: 24805245]
21. Villa F, Simon AC, Ortiz Bazan MA, Kilkenny ML, Wirthensohn D, Wightman M, Matak-Vinkovic D, Pellegrini L, and Labib K (2016). Ctf4 Is a Hub in the Eukaryotic Replisome that Links Multiple CIP-Box Proteins to the CMG Helicase. Mol Cell 63, 385–396. 10.1016/j.molcel.2016.06.009. [PubMed: 27397685]
22. Singleton MR, Dillingham MS, and Wigley DB (2007). Structure and mechanism of helicases and nucleic acid translocases. Annu Rev Biochem 76, 23–50. [PubMed: 17506634]
23. Leonaite B, Han Z, Basquin J, Bonneau F, Libri D, Porrua O, and Conti E (2017). Sen1 has unique structural features grafted on the architecture of the Upf1-like helicase family. EMBO J 36, 1590–1604. 10.15252/embj.201696174. [PubMed: 28408439]
24. Han Z, Libri D, and Porrua O (2017). Biochemical characterization of the helicase Sen1 provides new insights into the mechanisms of non-coding transcription termination. Nucleic Acids Res 45, 1355–1370. 10.1093/nar/gkw1230. [PubMed: 28180347]
25. Martin-Tumasz S, and Brow DA (2015). Saccharomyces cerevisiae Sen1 Helicase Domain Exhibits 5'- to 3'-Helicase Activity with a Preference for Translocation on DNA Rather than RNA. J Biol Chem 290, 22880–22889. 10.1074/jbc.M115.674002. [PubMed: 26198638]
26. Schellenberg MJ, Petrovich RM, Malone CC, and Williams RS (2018). Selectable high-yield recombinant protein production in human cells using a GFP/YFP nanobody affinity support. Protein Sci 27, 1083–1092. 10.1002/pro.3409. [PubMed: 29577475]
27. Chakrabarti S, Jayachandran U, Bonneau F, Fiorini F, Basquin C, Domcke S, Le Hir H, and Conti E (2011). Molecular mechanisms for the RNA-dependent ATPase activity of Upf1 and its regulation by Upf2. Mol Cell 41, 693–703. 10.1016/j.molcel.2011.02.010. [PubMed: 21419344]
28. Lim SC, Bowler MW, Lai TF, and Song H (2012). The Ighmbp2 helicase structure reveals the molecular basis for disease-causing mutations in DMSA1. Nucleic Acids Res 40, 11009–11022. 10.1093/nar/gks792. [PubMed: 22965130]
29. Lacabanne D, Wiegand T, Wili N, Kozlova MI, Cadalbert R, Klose D, Mulkidjanian AY, Meier BH, and Bockmann A (2020). ATP Analogues for Structural Investigations: Case Studies of a DnaB Helicase and an ABC Transporter. Molecules 25. 10.3390/molecules25225268.
30. Gao Y, and Yang W (2020). Different mechanisms for translocation by monomeric and hexameric helicases. Curr Opin Struct Biol 61, 25–32. 10.1016/j.sbi.2019.10.003. [PubMed: 31783299]
31. van Zundert GCP, Rodrigues J, Trellet M, Schmitz C, Kastritis PL, Karaca E, Melquiond ASJ, van Dijk M, de Vries SJ, and Bonvin A (2016). The HADDOCK2.2 Web Server: User-Friendly Integrative Modeling of Biomolecular Complexes. J Mol Biol 428, 720–725. 10.1016/j.jmb.2015.09.014. [PubMed: 26410586]
32. Saikrishnan K, Powell B, Cook NJ, Webb MR, and Wigley DB (2009). Mechanistic basis of 5'-3' translocation in SF1B helicases. Cell 137, 849–859. 10.1016/j.cell.2009.03.036. [PubMed: 19490894]
33. Lee JY, and Yang W (2006). UvrD helicase unwinds DNA one base pair at a time by a two-part power stroke. Cell 127, 1349–1360. 10.1016/j.cell.2006.10.049. [PubMed: 17190599]
34. Cheng Z, Muhlrad D, Lim MK, Parker R, and Song H (2007). Structural and functional insights into the human Upf1 helicase core. EMBO J 26, 253–264. 10.1038/sj.emboj.7601464. [PubMed: 17159905]
35. Unciuleac MC, Meir A, Xue C, Warren GM, Greene EC, and Shuman S (2021). Clutch mechanism of chemomechanical coupling in a DNA resecting motor nuclease. Proc Natl Acad Sci U S A 118. 10.1073/pnas.2023955118.
36. Warren GM, Meir A, Wang J, Patel DJ, Greene EC, and Shuman S (2022). Structure-activity relationships at a nucleobase-stacking tryptophan required for chemomechanical coupling in the DNA resecting motor-nuclease AdnAB. Nucleic Acids Res 50, 952–961. 10.1093/nar/gkab1270. [PubMed: 34967418]

37. Ashkenazy H, Abadi S, Martz E, Chay O, Mayrose I, Pupko T, and Ben-Tal N (2016). ConSurf 2016: an improved methodology to estimate and visualize evolutionary conservation in macromolecules. Nucleic Acids Res 44, W344–350. 10.1093/nar/gkw408. [PubMed: 27166375]
38. Jumper J, Evans R, Pritzel A, Green T, Figurnov M, Ronneberger O, Tunyasuvunakool K, Bates R, Zidek A, Potapenko A, et al. (2021). Highly accurate protein structure prediction with AlphaFold. Nature 596, 583–589. 10.1038/s41586-021-03819-2. [PubMed: 34265844]
39. Finkel JS, Chinchilla K, Ursic D, and Culbertson MR (2010). Sen1p performs two genetically separable functions in transcription and processing of U5 small nuclear RNA in Saccharomyces cerevisiae. Genetics 184, 107–118. 10.1534/genetics.109.110031. [PubMed: 19884310]
40. Ozgur S, Buchwald G, Falk S, Chakrabarti S, Prabu JR, and Conti E (2015). The conformational plasticity of eukaryotic RNA-dependent ATPases. Febs J 282, 850–863. 10.1111/febs.13198. [PubMed: 25645110]
41. Zheng SQ, Palovcak E, Armache JP, Verba KA, Cheng Y, and Agard DA (2017). MotionCor2: anisotropic correction of beam-induced motion for improved cryo-electron microscopy. Nat Methods 14, 331–332. 10.1038/nmeth.4193. [PubMed: 28250466]
42. Punjani A, Rubinstein JL, Fleet DJ, and Brubaker MA (2017). cryoSPARC: algorithms for rapid unsupervised cryo-EM structure determination. Nat Methods 14, 290–296. 10.1038/nmeth.4169. [PubMed: 28165473]
43. Punjani A, Zhang H, and Fleet DJ (2020). Non-uniform refinement: adaptive regularization improves single-particle cryo-EM reconstruction. Nat Methods 17, 1214–1221. 10.1038/s41592-020-00990-8. [PubMed: 33257830]
44. Bepler T, Morin A, Rapp M, Brasch J, Shapiro L, Noble AJ, and Berger B (2019). Positive-unlabeled convolutional neural networks for particle picking in cryo-electron micrographs. Nat Methods 16, 1153–1160. 10.1038/s41592-019-0575-8. [PubMed: 31591578]
45. Emsley P, Lohkamp B, Scott WG, and Cowtan K (2010). Features and development of Coot. Acta crystallographica. Section D, Biological crystallography 66, 486–501. 10.1107/S0907444910007493. [PubMed: 20383002]
46. Senior AW, Evans R, Jumper J, Kirkpatrick J, Sifre L, Green T, Qin C, Zidek A, Nelson AWR, Bridgland A, et al. (2020). Improved protein structure prediction using potentials from deep learning. Nature 577, 706–710. 10.1038/s41586-019-1923-7. [PubMed: 31942072]
47. Adams PD, Afonine PV, Bunkoczi G, Chen VB, Echols N, Headd JJ, Hung LW, Jain S, Kapral GJ, Grosse Kunstleve RW, et al. (2011). The Phenix software for automated determination of macromolecular structures. Methods 55, 94–106. 10.1016/j.ymeth.2011.07.005. [PubMed: 21821126]
48. Bouvette J, Huang Q, Riccio AA, Copeland WC, Bartesaghi A, and Borgnia MJ (2022). Automated systematic evaluation of cryo-EM specimens with SmartScope. Elife 11. 10.7554/eLife.80047.
49. Otwinowski Z, and Minor W (1997). Processing of X-ray diffraction data collected in oscillation mode. Methods Enzymol 276, 307–326. [PubMed: 27754618]

HIGHLIGHTS

- Sen1 (Senataxin, SETX) RNA-DNA helicase structure resembles an elongated inchworm.
- Sen1 is auto-regulated by the Sen1N domain that directly binds its helicase core.
- Sen1 helicase core RNA complex structures show the enzyme encircles RNA.
- AOA2 RNA binding cleft mutations undermine RNA-DNA unwinding activity.

INCLUSION AND DIVERSITY

One or more of the authors of this paper self-identifies as an underrepresented ethnic minority in science. We support inclusive, diverse, equitable conduct of research.

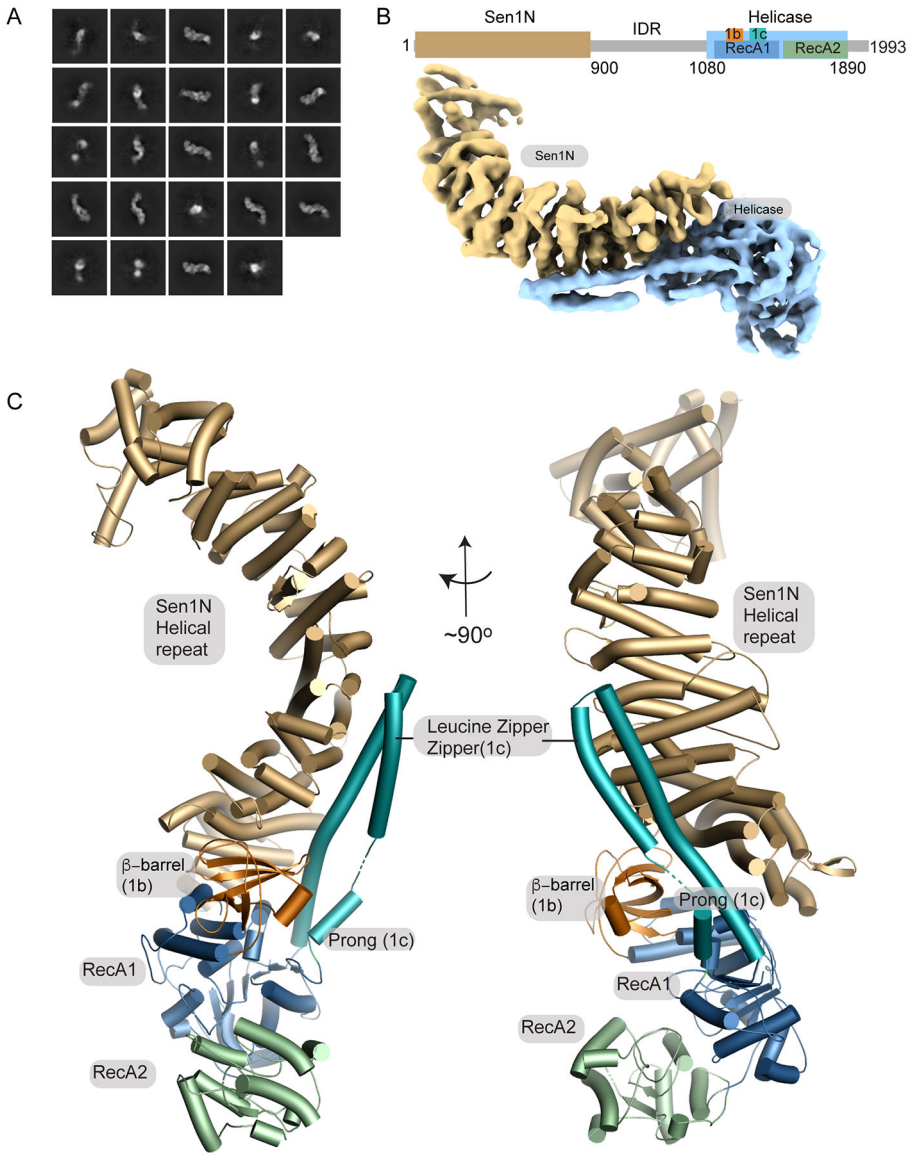

Figure 1. Cryo-EM structure of Sen1^{FL}

(A) 2D cryo-EM class averages of full-length Sen1 show an asymmetric elongated assembly.

(B) Cryo-EM volume of Sen1^{FL} is displayed showing the Sen1N domain in brown, and the helicase core in blue.

(C) The Sen1N helical repeat (tan). Extensive interactions with helical repeat are mediated by RecA1 1b (orange) and 1c (turquoise) insertion elements. The LZZ (RecA1 1c insertion) reinforces the interface.

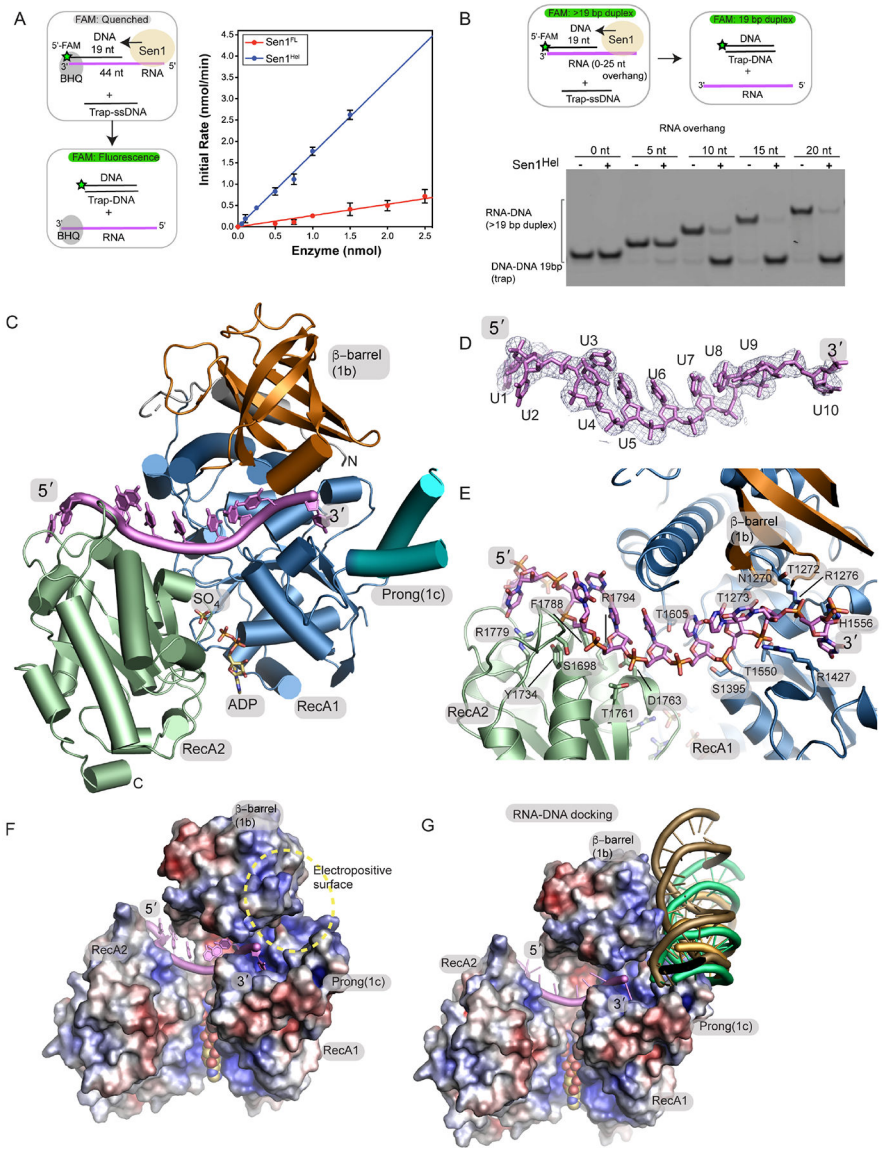

Figure 2. Crystal structure of the Sen1^{Hel}–ssRNA–ADP–SO_4 complex

(A) Left: RNA-DNA unwinding substrates. Right: Sen1^{FL} and Sen1^{Hel} at the amounts indicated were incubated with 50 nmol of Sub7 (Table S2). Reactions were initiated by addition of a mixture containing ATP (1 mM) and $MgCl_2$ (2 mM). FAM signal was detected at 520 nm every 10 sec over 30 min at 25 °C. Initial rates were determined by linear fit of the first 5 min of the unwinding reaction. Error bars are SD from 5 replicates.

(B) Top: gel-based RNA-DNA unwinding assay. Bottom: Effect of RNA overhang length on Sen1^{Hel} RNA-DNA unwinding activity. Sub1-Sub5 (Supplementary Table 3) at 20 nM, Sen1^{Hel} (50 nM), 19-Trap DNA (Table 1) at 200 nM, ATP (1 mM), $MgCl_2$ (2 mM) were incubated for 15 min at 37 °C.

(C) X-ray structure of the Sen1^{Hel}–RNA–ADP–SO_4 complex. The extended LZZ coiled coil is not shown.

(D) Composite Omit 2Fo-Fc electron density at 1.0 σ, carved 2.0 Å around the RNA chain.

(E) Sen1^{Hel} RNA-protein interactions show an extensive RNA binding interface.
(F) APBS surface electrostatic surface representation (blue=electropositive, red= electronegative) of the Sen1 RNA binding surface. Sen1 encircles the RNA via its RecA1 and RecA2 domains.
(G) Representative HADDOCK RNA-DNA poses displayed show secondary putative RNA-DNA hybrid binding electropositive surface flanks the ssRNA binding site and is assembled by the 1b and 1c RecA1 insertions.

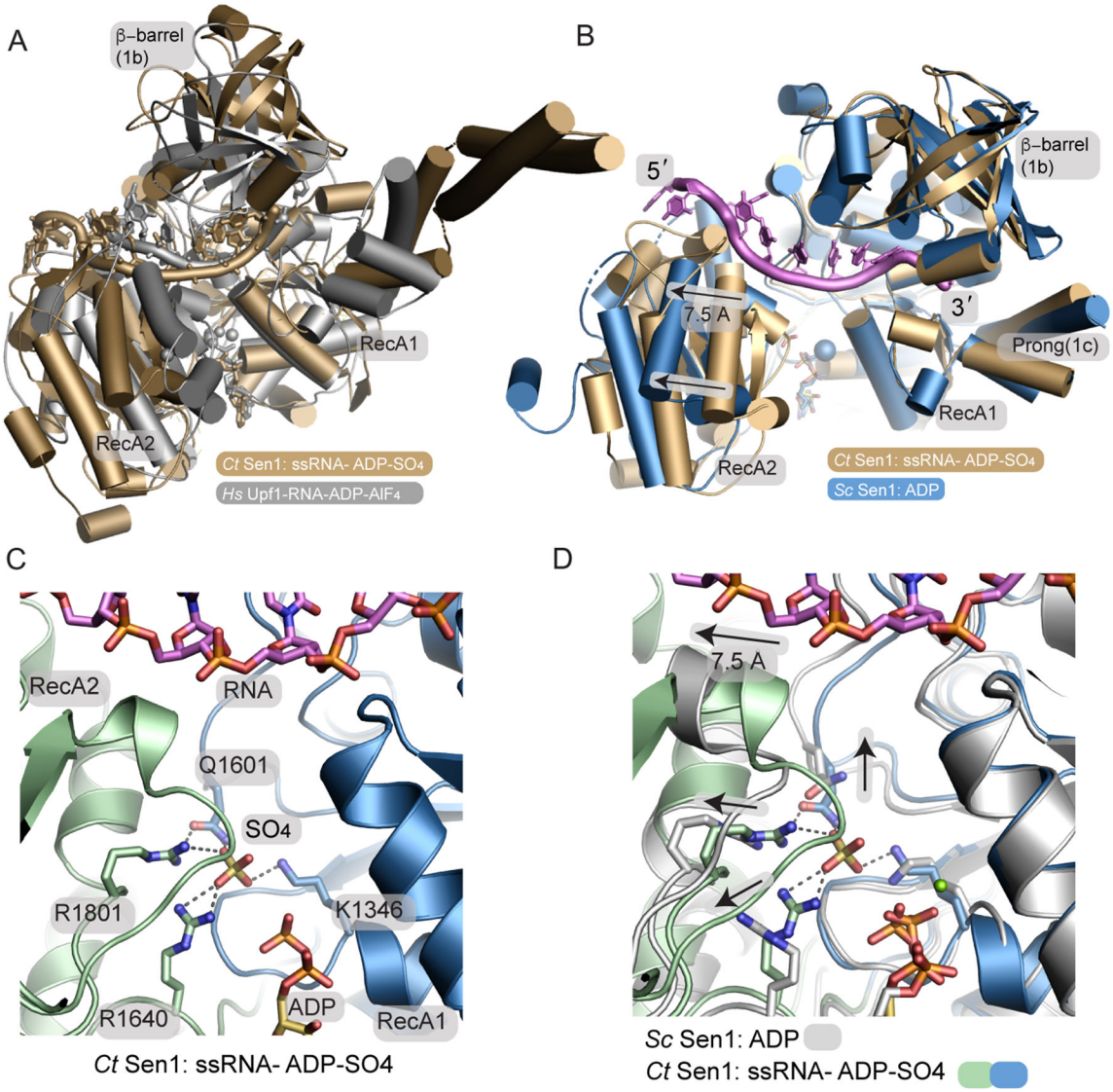

Figure 3. A phosphate sensor is a lynchpin in the Sen1 power stroke

(A) Structural superposition of the $Sen1^{Hel}$–RNA–ADP–SO_4 complex (tan) with the HsUpf1-RNA-ADP-AlF_4 complex (grey).

(B) Structural superposition of the Sen1-RNA-ADP-$S0_4$ complex with ScSen1-ADP-Mg^{2+} complex, RSCB:5MZN. Close superposition of the RecA1 domains is observed. A 7.5 Å translocation is coincident with phosphate release. The blue sphere marks the position of Mg^{2+} in the ScSen1 -ADP-Mg^{2+} complex.

(C) Sen1 active site. Four residues from the RecA1 and RecA2 domains bind SO_4, a mimic of the hydrolyzed phosphate prior to phosphate release.

(D) Active site structural superposition of ScSen1-ADP and CtSen1-RNA-ADP-SO_4 complexes colored as indicated. Arrows show structural rearrangements of conserved gamma-phosphate sensing residues upon phosphate (SO_4 mimic) release.

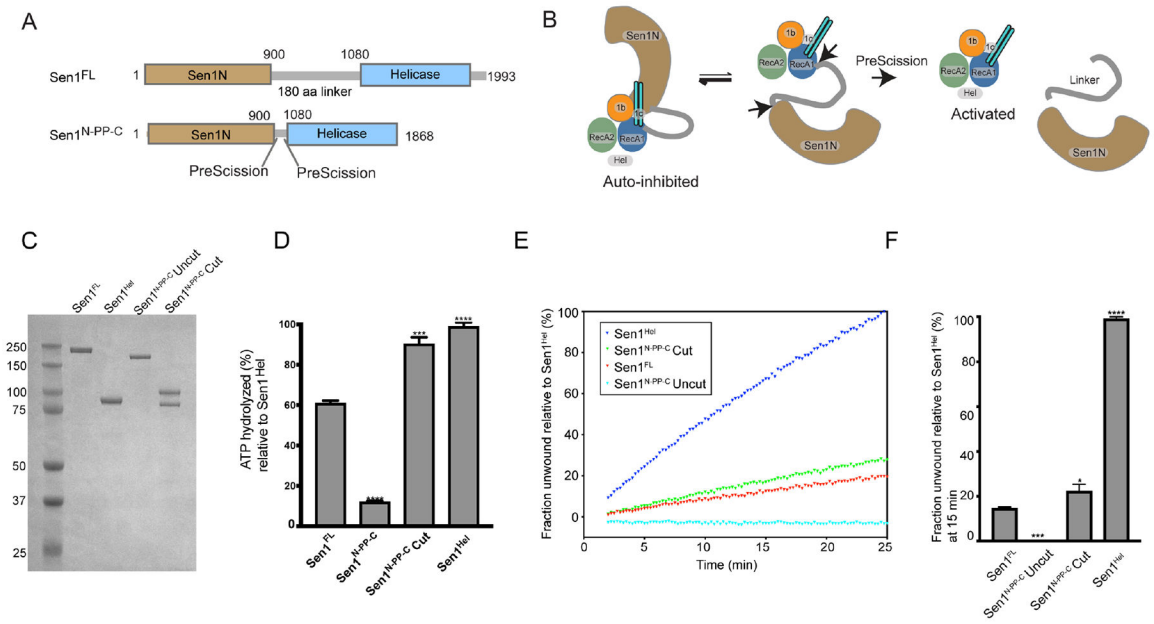

Figure 4. The Sen1N domain is autoinhibitory.

(A) Design of a PreScission Protease cleavable Sen1.

(B) Schematic of activation of PreScission Protease cleavable Sen1$^{N\text{-}PP\text{-}C}$.

(C) Purified Sen1 proteins or PreScission Protease cleaved protein (Sen1$^{N\text{-}PP\text{-}C}$ – Cut) used in panels D–F.

(D) Substrate stimulated ATP hydrolysis of mutant Sen1 proteins was monitored in a phosphate release assay. Sen1^{FL}, Sen1$^{N\text{-}PP\text{-}C}$ (Uncut), PreScission Protease-cleaved Sen1N-PP-C (Cut) and Sen1Hel (5 nM) were incubated with Sub6 (Supplementary Table 3) at 5 μM and ATP (1 mM) and MgCl2 (2 mM) for 15 min at 37 °C. Error bars are SD from 3 replicates, ***p<0.001, **** p<0.0001.

(E) Helicase assay of indicated Sen1 protein (1 nM) was performed as in Figure 2A and normalized to unwound fraction of Sen1^{Hel} for comparison.

(F) Comparison of unwound fractions at 25 min from experiments in “E”. Error bars are SD from 3 replicates. Statistical analysis was done using paired t-test relative to Sen1^{FL}. *p<0.05, ***p<0.001, ****p<0.0001.

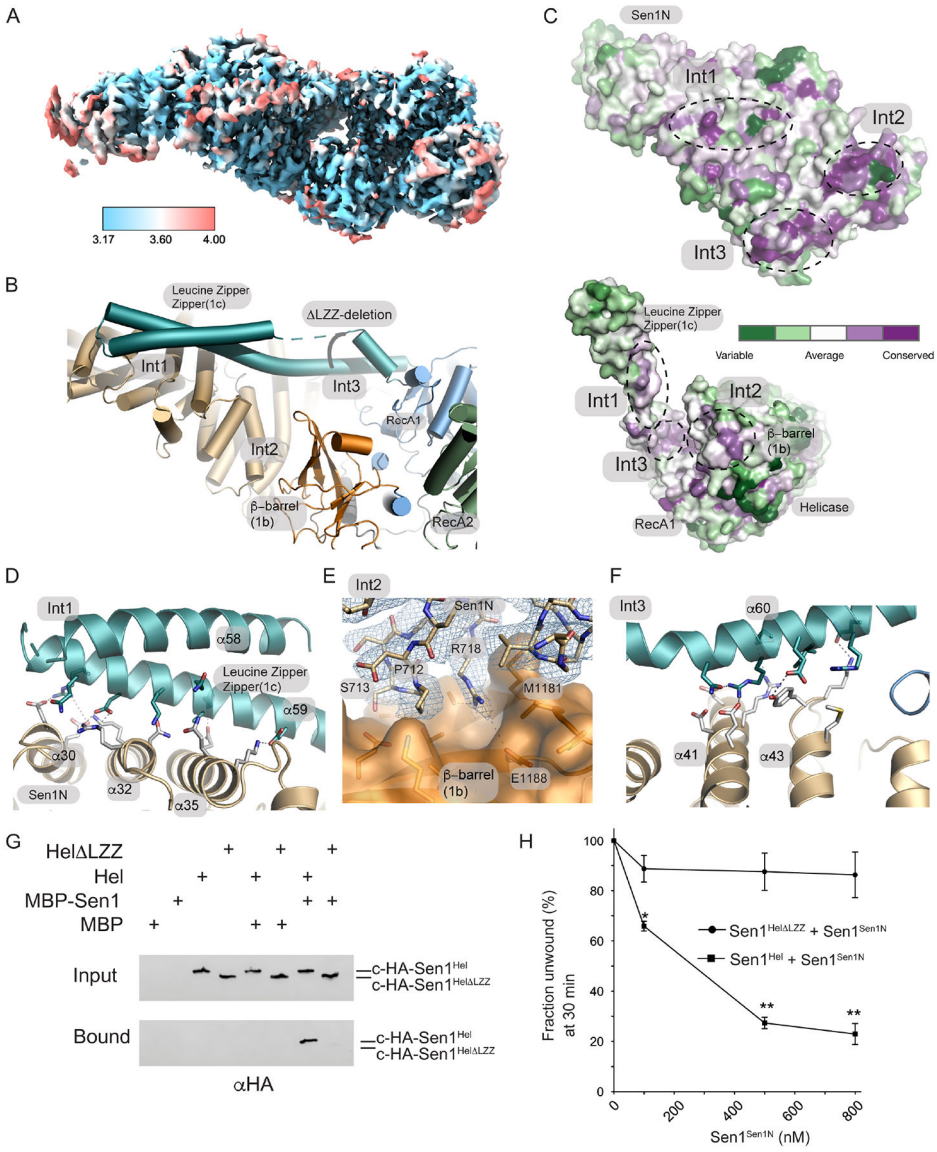

Figure 5. Cryo-EM structure of Sen1$^{N\text{-}PP\text{-}C}$

(A) Local resolution of Sen1$^{N\text{-}PP\text{-}C}$, calculated in using the Local Resolution Estimation in CryoSparc, and displayed using a blue (high-resolution, 3.17 Å) to red (low-resolution, 4.0 Å) color-coded surface.

(B) Three interaction interfaces (Int1-Int3) mediate Sen1^{Sen1N} interaction with Sen1^{Hel}. The LZZ from Sen1^{Hel} binds both Int1 and Int3 on Sen1^{Sen1N}. A ΔLZZ internal deletion construct is marked.

(C) Consurf analysis of the Sen1^{Sen1N} surface reveals conserved surface interaction interfaces (Int1-Int3, dotted lines) are involved in interactions with Sen1^{Hel}. Top: Sen1N domain interaction interfaces that bind the helicase domain. Bottom: Helicase domain interaction surfaces that bind the Sen1N domain.

(D) Molecular details of the Int1 interdomain Sen1^{Sen1N} - Sen1^{Hel} interaction interface.

(E) Cryo-EM density for $Sen1^{Sen1N}$ Int2 region displayed contoured at 11.0 σ overlaid upon a molecular surface diagram of the β-barrel domain (orange).
(F) Molecular details of the Int3 interdomain $Sen1^{Sen1N}$ - $Sen1^{Hel}$ interaction interface.
(G) MBP-pulldowns show the LZZ is critical for the $Sen1^{Sen1N}$–$Sen1^{Hel}$ interaction.
(H) Trans inhibition of $Sen1^{Hel}$ by $Sen1^{Sen1N}$. $Sen1^{Hel}$ (1 nM) was pre-incubated with $Sen1^{Sen1N}$ at the indicated concentrations for 5 min on ice. Reactions were initiated by addition of 50 nM Sub7 (Supplementary Table 3) and a mixture containing ATP (1 mM) and $MgCl_2$ (2 mM). The percentage of unwound ssDNA was calculated from the FAM signal at 30 min. Error bars are SD from 3 replicates, **p<0.01, *p<0.05.

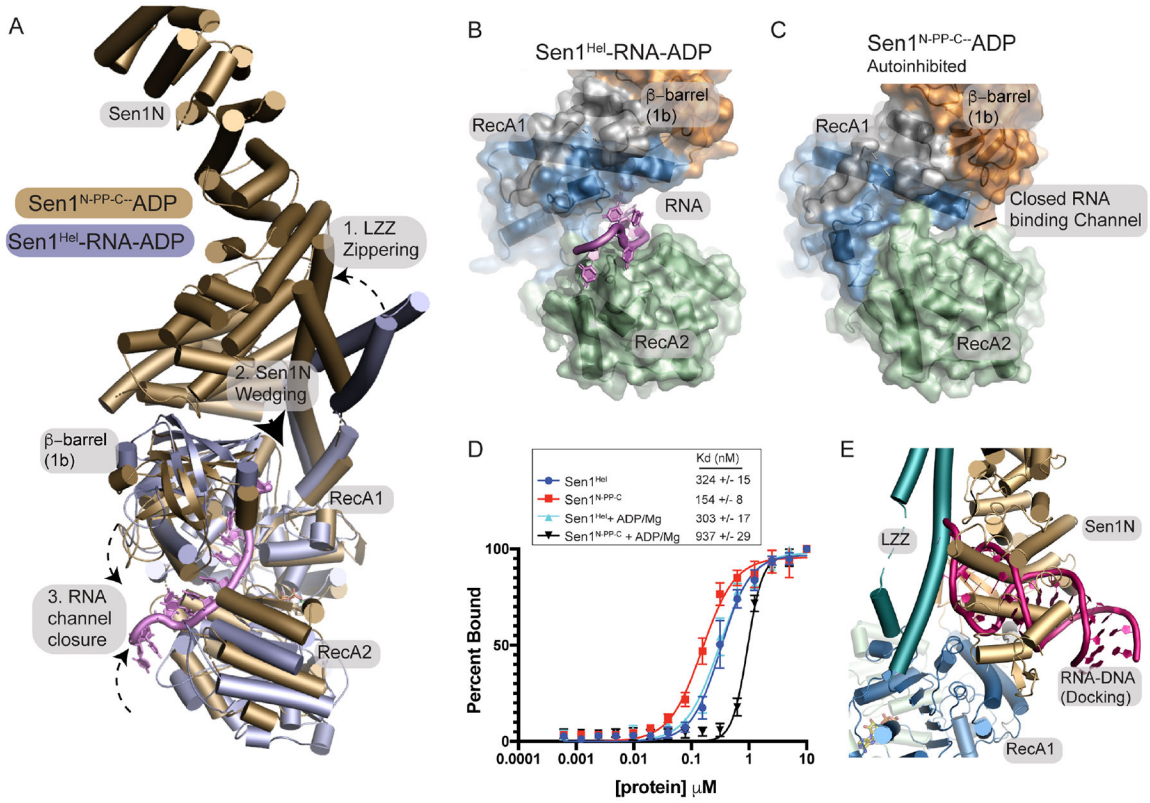

Figure 6. Mechanism of Sen1 auto-inhibition

(A) Structural superposition of Sen1$^{N\text{-}PP\text{-}C}$ and the Sen1^{Hel} RNA complex reveals a cascade of conformational rearrangements associated with autoinhibition.

(B) Surface diagram of the Sen1-RNA complex and Sen1$^{N\text{-}PP\text{-}C}$ shows alterations in the RNA binding channel in the closed state “C”.

(D) Fluorescence polarization ssRNA binding. Binding to ssRNA was conducted using enzyme titration and monitoring fluorescence polarization from Sub8 (Supplementary Table 3. Error bars reflect SD from 3 replicates.

(E) Superposition of an example HADDOCK docking binding pose and the autoinhibited Sen1$^{N\text{-}PP\text{-}C}$ state.

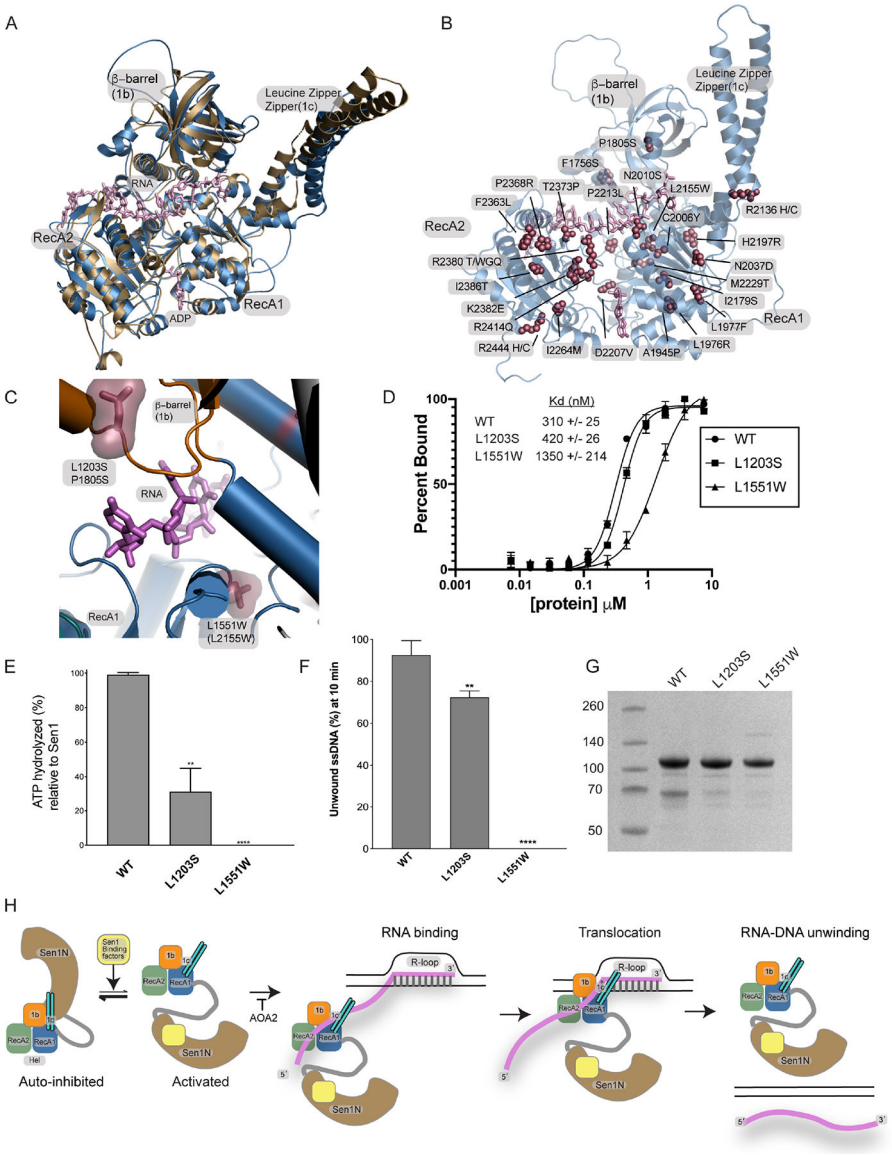

Figure 7. AOA2 mutants Sen1 RNA binding mechanism

(A) Structural overlay of an Alphafold model of human SETX helicase domain (blue) with the CtSen1 RNA complex (tan).

(B) Alphafold model of the hSETX helicase domain showing the location of mapped AOA2 and ALS4 mutations

(C) Two AOA2 mutations map to the RNA binding cleft. Human equivalent positions are shown below the CtSen1 numbering in parentheses and the CtSen1 structure is displayed.

(D) Fluorescence polarization ssRNA binding. Binding to ssRNA was conducted using enzyme titration and monitoring fluorescence polarization from Sub8 (Supplementary Table 3). Error bars reflect SD from 3 replicates.

(E) ATPase activity. Proteins (5 nM) were incubated with Sub6 (Supplementary Table 3) and ATP (1 mM) at 5 μM for 15 min at 37 °C. The L1551W mutant had no measurable activity. Error bars are SD from 3 replicates, **p<0.01, ****p<0.0001.

(F) RNA—DNA unwinding activity. Proteins (1 nM) were incubated with 50 nM Sub7 (Supplementary Table 3), ATP (1 mM) and $MgCl_2$ (2 mM). FAM signal at 10 min was used to compare the unwinding activities of $Sen1^{Hel}$ mutants. The L1551W mutant had no measurable activity. Error bars are SD from 3 replicates, **p<0.01, ****p<0.0001.
(G) Purified $Sen1^{Hel}$ proteins used in panels B–D.
(H) Model for Sen1 autoinhibition and RNA translocation.

Table 1.

Cryo-EM data collection and refinement statistics

	Sen1^{FL}	**Sen1^{Sen1N}**	**Sen1^{N-PP-C}**
EMDB	EMD-29439	EMD-29440	EMD-29426
PDB ID	8FTK	n/a	8FTH
Data collection and processing			
Microscope	Titan Krios	Titan Krios	Titan Krios
Detector	K2 summit	K2 summit	Gatan3 Bioquantum
Magnification	130,000	130,000	130,000
Voltage(kV)	300	300	300
Electron exposure (e–/Å2)	60	60	40
Defocus range (μm)	−1.4 to −2.2	−1.4 to −2.2	−1.0 to −2.7
Pixel size (Å)	0.53	0.53	0.67
Symmetry imposed	C1	C1	C1
Number of micrographs	5089	5089	6379 (set1) + 3655 (set2)
Initial particle images (no.)	1351862	1351862	3400325 (set1) + 3273289 (set2)
Final particle images (no.)	29391	74760	471395
Map resolution - unmaksed (Å) (FSC = 0.143)	7.40	6.86	3.69
Map resolution -masked (Å) (FSC = 0.143)	4.56	4.49	3.17
Refinement			
Initial models used (PDB code)	AlphaFold (1-900), CtSen1^{Hel} X-ray	No model refined	AlphaFold (1-900), CtSen1^{Hel} X-ray
Map sharpening B factor (Å^2)	122.6		142.5
Model composition	Polyalanine		
Nonhydrogen atoms	7840		9778
Protein residues	1584		1263
ADP nucleotides	0		1
B factors (Å2) (mean)			
Protein	219.90		56.70
Nucleotide	n/a		40.90
R.M.S. deviations			
Bond lengths (Å)	0.002		0.008
Bond angles (°)	0.573		1.266
Map-model CC			
CC (mask)	0.81		0.75
CC (volume)	0.80		0.72
CC (peaks)	0.74		0.61

	Sen1^{FL}	Sen1^{Sen1N}	Sen1^{N-PP-C}
Validation			
Molprobity score	1.60		1.60
Clashscore	4.21		4.89
Poor rotamers (%)	0.00		0.49
Ramachandran plot			
Outliers (%)	0.00		0.00
Allowed (%)	5.86		4.87
Favored (%)	94.14		95.13

Table 2.

X-ray data collection and refinement statistics

PDB code: 8FTM	**SEN1^{Hel}-RNA-ADP-SO$_4$**
Wavelength (Å)	1.000
Resolution range (Å)	50-3.0
Space group	$P2_1$
Unit cell	a=56.705 b=107.323 c=162.029 β=99.64
Total reflections	258925
Multiplicity	6.9 (6.9)
Completeness (%)	99.1 (99.5)
Mean I/sigma(I)	11.4 (1.3)
CC1/2	0.999 (0.872)
CC*	1.000 (0.965)
R-meas	0.121 (0.725)
R-work	0.212 (0.310)
R-free	0.251 (0.348)
Number of non-hydrogen atoms	11842
Protein residues	1445
RNA nucleotides	22
Ligands (ADP, SO_4)	10
Water molecules	6
Protein residues	1428
RMS(bonds)	0.002
RMS(angles)	0.52
Ramachandran favored (%)	96.01
Ramachandran allowed/outliers (%)	3.99/0.00
Average B-factor (overall)	91.08
Protein	90.87
RNA	96.11
Ligands (ADP, SO_4)	102.20
Water	55.71

Statistics for the highest-resolution shell are shown in parentheses.

Key Resource Table

REAGENT or RESOURCE	SOURCE	IDENTIFIER
Antibodies		
Rabbit Anti-MBP	GeneTex	GTX124267
Mouse Anti-HA	GeneTex	GTX628489
IRDye680 Goat Anti Rabbit	LI-COR	926-68071
IRDye800 Goat Anti Mouse	LI-COR	926-32210
Bacterial and virus strains		
BL21-AI *E. coli*	Invitrogen	Cat# C607003
HEK 293 Freestyle	Thermo Fisher	Cat# R79007
Chemicals, peptides, and recombinant proteins		
L-Arabinose	GoldBio	A-300-25
Lipofectamine ™ 2000 Transfection Reagent	Thermo Fisher	11668019
Recombinant CtSen1^{FL} (full length)	This paper	N/A
Recombinant CtSen1$^{N\text{-}PP\text{-}C}$ (1-900-PreScission-PreScission-1080-1868)	This paper	N/A
Recombinant CtSen1^{Sen1N} (1-900)	This paper	N/A
Recombinant CtSen1^{Hel} (1087-1890)	This paper	N/A
Recombinant CtSen1$^{Hel\Delta LZZ}$ (1087(Δ1457-1525)-1890)	This paper	N/A
Recombinant CtSen1$^{Hel\text{-}1878}$ (1087-1878)	This paper	N/A
Recombinant CtSen1^{Hel} mutants (L1203S and L1551W)	This paper	N/A
Critical commercial assays		
QuickChange Site-Directed Mutagenesis Kit	Agilent	200519
Q5 Mutagenesis Kit	NEB	E0552S
Malachite Green Phosphate Assay Kit	Cayman	10009325
Deposited data		
CtSen1^{FL}, cryo-EM map and refined coordinates	This paper	EMD: 29439, PDB: 8FTK
CtSen1^{Sen1N}, cryo-EM map	This paper	EMD: 29440
CtSen1$^{N\text{-}PP\text{-}C}$, cryo-EM map and refined coordinates	This paper	EMD: 29426, PDB: 8FTH
CtSen1^{Hel}-RNA-ADP-SO_4, X-ray data and refined coordinates	This paper	PDB: 8FTM
Uncropped gels, Mendeley data	This paper	doi:10.17632/djm6wdc5tg.1
Oligonucleotides		
CtSen1^{Hel} L1203S-fwd (AGTAAGGATCGCGGTAGTACCGAAGGCGACATC)	This paper	N/A
CtSen1^{Hel} L1203S-rev (GATGTCGCCTTCGGTACTACCGCGATCCTTACT)	This paper	N/A
CtSen1^{Hel} L1551W-fwd (GTTCTGTGTGCCACGTGGAGTGGCAGCGGCCAC)	This paper	N/A
CtSen1^{Hel} L1551W-rev (GTGGCCGCTGCCACTCCACGTGGCACACAGAAC)	This paper	N/A
CtSen1$^{Hel\text{-}1878}$-fwd (GTGGAAATGCACGACTAATGACGTACGAGTGAA)	This paper	N/A
CtSen1$^{Hel\text{-}1878}$-rev (TTCACTCGTACGTCATTAGTCGTGCATTTCCAC)	This paper	N/A

REAGENT or RESOURCE	SOURCE	IDENTIFIER
CtSen1$^{Hel\text{-}cHA}$-fwd (GCCGGATTATGCGTAATGAAAGGGTGGGCGCGC)	This paper	N/A
CtSen1$^{Hel\text{-}cHA}$-rev (ACATCATACGGATATGGCATCGCCGGCGGGAT)	This paper	N/A
Substrate oligos for RNA-DNA unwinding assays	Supplementary Table 3	N/A
Substrate oligos for ATPase assays	Supplementary Table 2	N/A
Substrate oligos for EMSAs	Supplementary Table 3	N/A
Substrate RNAs for crystallization	Supplementary Table 2	N/A
Substrate RNA for fluorescence polarization RNA binding	Supplementary Table 2	N/A
Recombinant DNA		
CtSen1^{FL} (full length)	This paper	N/A
CtSen1$^{N\text{-}PP\text{-}C}$ (1-900-PreScission-PreScission-1080-1868)	This paper	N/A
CtSen1^{Sen1N} (1-900)	This paper	N/A
CtSen1^{Hel} (1087-1890)	This paper	N/A
CtSen1^{HelΔLZZ} (1087(Δ1457-1525)-1890)	This paper	N/A
CtSen1$^{Hel\text{-}1878}$ (1087-1878)	This paper	N/A
CtSen1^{Hel} mutants (L1203S and L1551W)	This paper	N/A
Software and algorithms		
PHENIX	Adams et al.[47]	N/A
Coot	Emsley and Cowtan[45]	N/A
HKL-2000	HKL Research Inc.	N/A
PyMOL	Schrödinger	N/A
Prism 8.0	GraphPad	N/A
TOPAZ	Bepler et al.[44]	N/A
Emperia Imaging Software	LI-COR	N/A
AlphaFold	Senior et al.[46]	N/A
CryoSparc v2.7	Punjani et al.[42] and Punjani et al.[43]	N/A
MotionCorr2	Zheng et al.[41]	N/A
Smartscope	Bouvette et al.[48]	N/A